

Model-independent constraints on superfluidity from the cooling neutron star in Cassiopeia A

Peter S. Shternin,^{1*} Dmitry D. Ofengeim,¹ Wynn C. G. Ho,² Craig O. Heinke,³ M.J.P. Wijngaarden⁴ and Daniel J. Patnaude⁵

¹*Ioffe Institute, Politekhnicheskaya 26, St. Petersburg, 194021, Russia*

²*Department of Physics and Astronomy, Haverford College, 370 Lancaster Avenue, Haverford, PA, 19041, USA*

³*Department of Physics, University of Alberta, CCIS 4-181, T6G 2E1, Edmonton, Alberta, Canada*

⁴*Mathematical Sciences and STAG Research Centre, University of Southampton, SO17 1BJ, Southampton, UK*

⁵*Smithsonian Astrophysical Observatory, Cambridge, MA 02138, USA*

Accepted XXX. Received YYY; in original form ZZZ

ABSTRACT

We present a new model-independent (applicable for a broad range of equations of state) analysis of the neutrino emissivity due to triplet neutron pairing in neutron star cores. We find that the integrated neutrino luminosity of the Cooper Pair Formation (CPF) process can be written as a product of two factors. The first factor depends on the neutron star mass, radius and maximal critical temperature of neutron pairing in the core, T_{Cnmax} , but not on the particular superfluidity model; it can be expressed by an analytical formula valid for many nucleon equations of state. The second factor depends on the shape of the critical temperature profile within the star, the ratio of the temperature T to T_{Cnmax} , but not on the maximal critical temperature itself. While this second factor depends on the superfluidity model, it obeys several model-independent constraints. This property allows one to analyse the thermal evolution of neutron stars with superfluid cores without relying on a specific model of their interiors. The constructed expressions allow us to perform a self-consistent analysis of spectral data and neutron star cooling theory. We apply these findings to the cooling neutron star in the Cassiopeia A supernova remnant using 14 sets of observations taken over 19 years. We constrain T_{Cnmax} to the range of $(5 - 10) \times 10^8$ K. This value depends weakly on the equation of state and superfluidity model, and will not change much if cooling is slower than the current data suggest. We also constrain the overall efficiency of the CPF neutrino luminosity.

Key words: dense matter – stars:neutron – neutrinos – supernovae: individual: Cassiopeia A – X-rays:stars

1 INTRODUCTION

The neutron star (NS) in the centre of the Cassiopeia A supernova remnant (hereafter CasA NS) was discovered in 1999 in the *Chandra* first light observations (Tananbaum 1999; Pavlov et al. 2000). The Cassiopeia A supernova is the most recent core-collapse supernova known in the Galaxy, possibly observed by John Flamsteed in 1680 (Ashworth 1980), although this evidence is not certain (e.g., Green & Stephenson 2003, and references therein). Nevertheless, the remnant kinematics points to the date of the explosion of 1681 ± 19 , making the remnant and the associated NS approximately 340 yr old (Fesen et al. 2006). The distance to the remnant is estimated as $3.4^{+0.3}_{-0.1}$ kpc (Reed et al. 1995).

In the last decade, the CasA NS received considerable attention due to two peculiar properties. First, its X-ray spectrum is thermal,

shows little or no pulsations and can be described by the emission from the whole NS surface if a carbon atmosphere is assumed (Ho & Heinke 2009; see also Chang, Bildsten & Arras 2010; Wijngaarden et al. 2019). It was the first NS for which the carbon atmosphere model had been successfully applied; several more such sources are known now (see, e.g., Klochov et al. 2013, 2016; Doroshenko et al. 2018; Hebbar et al. 2020; Ho et al. 2021). Second, the star probably shows real-time cooling, much faster than expected from the standard NS cooling models. Initially, a temperature decline of 3.9 ± 0.7 per cent in 10 yr (and 21 per cent X-ray flux decrease over the same period) was reported (Heinke & Ho 2010). Subsequent observations presented by Shternin et al. (2011); Elshamouty et al. (2013); Ho et al. (2015) confirmed this trend, albeit at a lower rate. Recently, Wijngaarden et al. (2019); Ho et al. (2021) reported another five *Chandra* observations, thus expanding the dataset to 14 sets of observations and extending the time span to ≈ 19 yr. They measured a temperature decline of 2.2 ± 0.2 per cent in 10

* E-mail: pshternin@gmail.com

yr (2.8 ± 0.3 per cent in 10 yr) if the interstellar absorption is set fixed (variable) between the epochs. The observations described above were taken using the *Chandra* ACIS-S GRADED mode. It was pointed out that this observing mode potentially can suffer from instrumental effects (Posselt et al. 2013), although revised *Chandra* Calibration Databases (CALDBS, Fruscione et al., 2006) over the years make efforts to account for these effects. Using three observations spanning 8.5 yr in the better-suited *Chandra* ACIS-S FAINT mode, Posselt & Pavlov (2018) found less significant cooling of 1.05 ± 0.44 per cent in 10 yr (1.6 ± 0.6 per cent in 10 yr) again for fixed (variable) interstellar absorption. Nevertheless, even a 1 per cent temperature decrease over 10 yr is too fast for the standard slow cooling of a NS that cools via neutrino emission mechanisms like the modified Urca process or nucleon bremsstrahlung (e.g., Yakovlev & Pethick 2004), which can lead only to about ~ 0.3 per cent temperature decline in 10 yr.

The standard explanation of the rapid CasA NS cooling assumes enhanced neutrino emissivity associated with the recent onset of the neutron superfluidity in the NS core (Page et al. 2011; Shternin et al. 2011). When the temperature in some part of the core falls below the critical temperature T_{Cn} of the superfluidity transition, neutrons start to form Cooper pairs. In this exothermic process, a fraction of energy is released in the form of neutrino-antineutrino pairs which are radiated away and thus cool the star (Flowers, Ruderman & Sutherland 1976). This mechanism is known as neutrino emission due to Cooper pairing formation (CPF) (the term ‘pair breaking and formation’ – PBF – emissivity is also frequently used in this context, to stress that, at a finite temperature, Cooper pairs not only form but also constantly break apart). The strength of the CPF emission is maximal at temperatures $T \approx 0.8T_{Cn}$, and it rapidly decreases at $T \lesssim 0.4T_{Cn}$.

Thus the suggested rapid cooling may provide direct evidence of the presence of superfluidity in NS interiors. Within this model, it is possible to constrain its characteristics, notably the maximal critical temperature of triplet neutron pairing in the core, $T_{Cn\max}$ [the critical temperature is density dependent, $T_{Cn} = T_{Cn}(\rho)$] (Page et al. 2011; Shternin et al. 2011), strength of the CPF emission (e.g., Shternin et al. 2011; Shternin & Yakovlev 2015) and the NS cooling rate prior to the neutron superfluidity onset. The latter rate is found to be considerably smaller than the typical standard cooling rate a NS would have. This is explained by the presence of the singlet proton superfluidity in the core with a relatively high critical temperature of $T_{Cp} \gtrsim 2 \times 10^9$ K. Such superfluidity suppresses the main neutrino emission processes, most importantly the Urca (direct and modified) processes (Page et al. 2011; Shternin et al. 2011). Notice that the CPF neutrino emission from the singlet proton pairing is negligible (e.g., Leinson 2018). The presence of the singlet proton and triplet neutron paired phases in the cores of NSs is a standard paradigm of NS physics (e.g., Haskell & Sedrakian 2018). Therefore the proposed explanation was natural as it had employed standard concepts of the NS cooling theory (Page et al. 2004, 2009; Gusakov et al. 2004).

There exist alternative explanations for the rapid cooling of the CasA NS. These include: delayed internal crust-core relaxation due to suppressed thermal conductivity in the core in the framework of the so-called ‘medium-modified cooling scenario’ (Blaschke et al. 2012; Blaschke, Grigorian & Voskresensky 2013; Grigorian, Blaschke & Voskresensky 2014); another sort of phase transition associated with an increase of neutrino luminosity roughly at the same internal temperature as in the original explanation but in a star with a quark core, i.e. the transition from the 2SC phase of quark matter to the crystalline SC phase (Sedrakian 2013) (notice

that the theoretical estimates of the temperature for these kind of transitions are ~ 100 times larger than those required for explaining the CasA NS cooling in this model); cooling after the end of an additional heating episode related to the dissipation of r-modes (Yang, Pi & Zheng 2011) or turbulent magnetic field (Bonanno et al. 2014); onset of the powerful direct Urca process in the central part of the star due to composition changes governed by the stellar spindown (Negreiros, Schramm & Weber 2013) (although this requires \sim ms initial rotation periods for the CasA NS, which is unlikely). We do not analyse these alternative scenarios here.

Here we assume that the CasA NS has cooled detectably via the standard mechanism. We aim to explore the range of NS cooling models that are compatible with the current update of the observational data and how these models can change in the future.

Modelling of the (superfluid) neutron star cooling relies on many microphysical ingredients, such as the equation of state (EOS), composition and thermodynamic properties of the superdense matter in NS interiors, rates of neutrino emission processes, superfluid critical temperature profiles, etc. On top of that, each microscopic model results in a family of cooling tracks/histories which are parameterized by the mass M of the star (or, equivalently the central density). For a given EOS, a specific M corresponds to some specific NS radius R . On the other hand, the NS atmosphere emission models, which are used to fit the observational data, also depend on M and R , and this dependence is not negligible. In principle, the stellar parameters used in the spectral analysis should be consistent with the parameters of the cooling models. This is not a straightforward task. In the initial studies of CasA NS cooling (Page et al. 2011; Shternin et al. 2011; Elshamouty et al. 2013; Shternin & Yakovlev 2015) this inconsistency was largely ignored. The first self-consistent study was performed by Ho et al. (2015) who considered a set of microphysical models and looked for the best-fit solution (if any) for each individual model. Ideally, the EOS, the critical density profiles and other microphysical quantities should be calculated within the same microscopic theory, however this is rarely available at present. Therefore, Ho et al. (2015) tested several EOSs supplemented with several critical temperature-density profiles available on the market; these two ingredients were considered to be decoupled. Only a few such combinations were able to provide consistent fits to CasA NS cooling data.

Here we propose a complementary alternative approach to perform the self-consistent spectral and cooling studies of CasA NS. Our approach is based on the approximate analytical expressions for the neutrino cooling rates which depend on mass and radius of the star but are largely independent on the EOS. Although being less exact for any specific model, this approach allows one to explore the whole parameter space, treat the spectral and cooling models self-consistently and obtain robust model-independent¹ constraints.

For the main neutrino emission processes that affect the evolution of *non-superfluid* neutron stars (with nucleon cores), i.e. direct and modified Urca processes as well as neutron-neutron bremsstrahlung, the appropriate analytical expressions were constructed by Ofengeim et al. (2017). These authors also provided similar expressions for the heat capacities. The constructed approximations are valid for a wide class of EOSs, allowing us to quantitatively compare the results of observations with the predictions of cooling theory for non-superfluid NSs in a model-independent way, taking into account correlations induced by M and R variations. These

¹ Model independent in terms of EOS and nucleon pairing but still within the framework of an overall scenario of superfluid nucleon NS cooling.

results have been applied to the analysis of the thermal state of a few sources (Yakovlev et al. 2011; Ofengeim et al. 2015; Ofengeim & Yakovlev 2017b; Ofengeim & Zyuzin 2018).

The construction of model-independent expressions for the CPF emission (required for application to CasA NS data) is less straightforward, since the CPF emission rate inevitably depends not only on the EOS, but also on the critical temperature profile $T_{Cn}(\rho)$. Nevertheless, as we show below, the integrated CPF neutrino luminosity can be represented as a product of two factors. The first one depends on M , R and $T_{Cn\max}$ but not on the shape of $T_{Cn}(\rho)$; it can be successfully approximated by universal expressions similar to those given by Ofengeim et al. (2017) for a broad range of EOSs. The second factor, in contrast, depends on the shape of the critical temperature profile but not on the absolute value of $T_{Cn\max}$. Roughly speaking, it characterises the fraction of the star which is superfluid at a given T . It depends on the EOS and the stellar model (i.e. M), but gives several model-independent constraints which we analyse in detail.

Applying the constructed expressions to the analysis of the CasA NS cooling data, we constrain the parameters of the neutron superfluidity. We find that the maximal redshifted neutron critical temperature within the core is $\tilde{T}_{Cn\max} = 4.5^{+1.1}_{-0.5} \times 10^8$ K [that corresponds to local $T_{Cn\max} \sim (5 - 10) \times 10^8$ K, in agreement with previous results, e.g. Shternin et al. 2011; Page et al. 2011], and this result does not depend on the spectral or interior model. We find, however, that the CPF neutrino emissivity should be at least twice as large as proposed by Leinson (2010).

The paper is organised as follows. In Section 2, we describe the spectral fits to the CasA NS data. In Section 3, we describe the basics of the superfluid neutron star cooling theory, construct the analytical expression for the CPF neutrino emission and describe its properties. In Section 4, we employ the constructed expression in the CasA NS cooling analysis. We discuss the results in Section 5, and conclude in Section 6.

2 CASA NS SPECTRAL ANALYSIS

We use *Chandra* ACIS-S GRADED mode observations, including the most recent observation from 2019 May 13. This is the same set of spectra as described in Ho et al. (2021), which are reprocessed with CIAO 4.13 using the latest CALDB 4.9.4 and then binned to ensure a minimum of 25 counts per energy bin. The data contain 14 observations² spanning 19 years from 2000 Jan to 2019 May (see Wijngaarden et al. 2019; Ho et al. 2021 for details).

All spectra are fitted simultaneously in the Bayesian framework using the affine-invariant Markov Chain Monte Carlo (MCMC) sampler EMCEE (Foreman-Mackey et al. 2013) which is connected to XSPEC v 12.9.0 (Arnaud 1996) via the Python wrapper PYXSPEC. We use χ^2 statistics as the likelihood for our data. We check that the use of the C -statistics (Cash 1979), with data binned by a minimum of 1 count per energy bin, gives similar results. We also find that the use of the C -statistics with unbinned spectra gives strongly biased results and cannot be used in our problem (see Appendix A for details).

The spectral model is the same as in Wijngaarden et al. (2019) and Ho et al. (2021) (see also Heinke & Ho 2010; Elshamouty et al.

2013) and contains a thermal component modelled by the non-magnetized carbon atmosphere model (NSX in XSPEC, Ho & Heinke 2009)³ modified by interstellar absorption (model TBABS, Wilms et al. 2000), dust scattering (model SPEXPCUT), and pileup (model PILEUP, Davis 2001). The parameters of the three latter model components are described in Wijngaarden et al. (2019). However, here we do not fix the grade migration parameters of the PILEUP model to the values found by Heinke & Ho (2010) (as done, e.g., by Wijngaarden et al. 2019), but allow them to vary. In contrast to Heinke & Ho (2010) and Ho et al. (2015, 2021), here we do not fix the grade migration parameters to be the same for observations with the same frame times but allow them to vary between all observations to more completely explore the parameter space.

The NS atmosphere model depends on the (non-redshifted) surface temperature T_s , NS mass M , radius R , and the normalization which is inversely proportional to the distance d to the star. Neutron star mass, radius and distance are the same for all observations. We do not fix the distance but use the informative prior on d which incorporates the distance uncertainty (see below). The surface temperature T_s and the hydrogen column density N_H of the TBABS model component are allowed to vary between observations. The *wilm* abundances for the photoelectric absorption model, from Wilms, Allen & McCray (2000), are used. For the surface temperature, we assume a power-law time dependence (see Section 3) already at the level of spectral fits using $\log T_s(t) = \log T_{s0} - s \log t/t_0$, where t is the NS age, calculated in such a way that $t_0 = 330$ yr corresponds to the MJD=55500 (Oct 2010), and s is the cooling slope. Therefore, the fit parameters include: $\log T_{s0}/(1 \text{ K})$, s , M , R , d and sets of column densities N_{Hi} and grade migration parameters α_i , $i = 1 \dots 14$. We also employ a second model, where all N_{Hi} are fixed to a single value N_{H0} .

The distance to the CasA NS is estimated as $d = 3.4^{+0.3}_{-0.1}$ kpc (Reed et al. 1995). Accordingly, in our spectral fits we set an informative Gaussian prior on d with the mean 3.4 kpc and the standard deviation 0.3 kpc (we symmetrise the uncertainties by increasing the lower boundary). We also set an informative prior on the column densities N_{Hi} , $i = 1 \dots 14$, assuming that they are sampled from the normal distribution with the mean N_{H0} and variance $\sigma_{N_H}^2$, where N_{H0} and $\sigma_{N_H}^2$ are the model hyperparameters. We assume a noninformative prior distribution $\sigma_{N_H}^2 > 0$ on the variance and a broad uniform prior $10^{21} \text{ cm}^{-2} < N_{H0} < 3 \times 10^{22} \text{ cm}^{-2}$ for the mean. For other parameters, we employ uniform priors in the ranges $-5 < s < 5$, $5.89 < \log_{10} T_{s0}/(1 \text{ K}) < 6.6$, $0.5 M_\odot < M < 3.0 M_\odot$, $1 \text{ km} < R < 30 \text{ km}$ and $0 < \alpha_i < 1$. We also do not allow acausal models (with $M/M_\odot > 0.24 R/(1 \text{ km})$, e.g., Lattimer & Prakash 2016) and parameter sets with surface gravity outside the range available for the NSX model⁴.

The fit is performed in the 0.5 – 7.0 keV spectral interval. The inferences on the model parameters for the models with variable N_H and fixed N_H are summarized in Table 1 (models 1 and 2 there, respectively). The inferences on the parameters α_i and N_{Hi} are not shown there, but are given in Table B2 in Appendix B. The details of the MCMC chains and the marginalized 1D and 2D posterior distributions of the fit parameters are given in Fig. B1 of Appendix B. All parameters for these two models are consistent within their errors, however the model with variable N_H might be

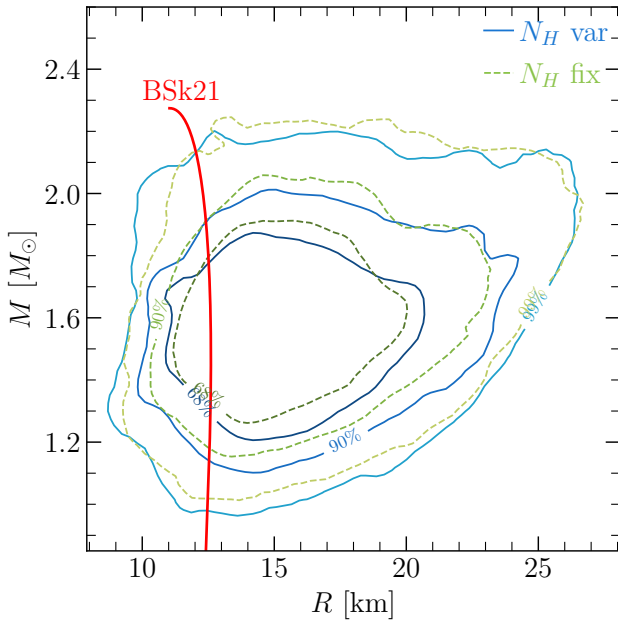
² Observations taken within a few days are merged together and treated as single observations.

³ We checked that another carbon atmosphere model, CARBATM (Suleimanov et al. 2014), available in XSPEC gives practically similar results.

⁴ https://www.slac.stanford.edu/~wynnho/nsx_models.dat

Table 1. Parameters of the spectral fit. Uncertainties correspond to the 68 per cent highest posterior density credible intervals.

Model	N_H	EOS	$\log_{10} T_{s0}/(1 \text{ K})$	s	M M_\odot	R km	d kpc	N_{H0} 10^{22} cm^{-2}	σ_{N_H} 10^{20} cm^{-2}	$\chi^2/\text{d.o.f.}$
1	Var	–	$6.216^{+0.034}_{-0.040}$	$0.61^{+0.10}_{-0.11}$	$1.55^{+0.21}_{-0.21}$	$14.8^{+3.4}_{-2.7}$	$3.40^{+0.35}_{-0.26}$	$1.621^{+0.045}_{-0.042}$	$3.6^{+1.8}_{-1.4}$	1613.3/1618
2	Fix	–	$6.215^{+0.038}_{-0.031}$	$0.54^{+0.08}_{-0.09}$	$1.59^{+0.21}_{-0.20}$	$14.8^{+3.0}_{-2.5}$	$3.43^{+0.32}_{-0.27}$	$1.634^{+0.040}_{-0.039}$	–	1640.2/1633
3	Var	BSk21	$6.262^{+0.013}_{-0.027}$	$0.66^{+0.10}_{-0.09}$	$1.57^{+0.16}_{-0.24}$	12.6	$3.35^{+0.24}_{-0.30}$	$1.643^{+0.039}_{-0.034}$	$3.6^{+1.6}_{-1.4}$	1614.5/1619
4	Fix	BSk21	$6.264^{+0.013}_{-0.026}$	$0.58^{+0.08}_{-0.08}$	$1.61^{+0.15}_{-0.24}$	12.6	$3.40^{+0.18}_{-0.35}$	$1.658^{+0.030}_{-0.035}$	–	1640.4/1634

**Figure 1.** Mass-radius credible contours obtained from our spectral fits. Solid and dashed contours correspond to models with variable and fixed N_H , respectively, and are labeled with their 68, 90 and 99 per cent credibility levels. The thick solid line indicates the $M - R$ relation for the BSk21 EOS.

statistically preferable over those with N_H being fixed (see, e.g., Wijngaarden et al. 2019; Ho et al. 2021).

The mass-radius credible contours (68 per cent, 90 per cent and 99 per cent credibility levels) inferred from the spectral models are shown in Fig. 1. The solid and dashed contours correspond to the models with variable and fixed N_H , respectively. The obtained $M - R$ range in Table 1 and Fig. 1 is somewhat higher but consistent with the standard values adopted for neutron stars and is compatible with the results from the *NICER* mission, which reported the NS radius of $13.02^{+1.24}_{-1.06}$ km (Miller et al. 2019) or $12.71^{+1.14}_{-1.19}$ km (Riley et al. 2019). The results on NS mass and radius are in agreement with those reported in Wijngaarden et al. (2019); Ho et al. (2021), although here we find a slightly more extended region for R . This can be attributed to the correlations between M , R and grade migration parameters α_i which are set free in the present work.

We also used models restricted to the specific EOS of the dense matter. For illustration, we selected one of the EOSs based on the Brussels-Skyrme nucleon interaction functionals, namely the BSk21 model (Potekhin et al. 2013). The $M - R$ relation for this EOS is shown in Fig. 1 with a thick solid line. For a $1.4 M_\odot$ NS, the BSk21 EOS gives $R \approx 12.6$ km. Technically, in the spectral fits we retained M as the fitting variable, while R was derived.

This resembles the analysis of Ho et al. (2015). The results for the BSk EOS are shown in Table 1 under the model numbers 3 and 4 (for variable and fixed N_H , respectively) and the corresponding marginalized posterior distributions are given in Fig. B2.

Thus, in this paper we analyse 4 spectral models. Investigating Table 1, one can conclude that the value of the cooling slope s is somewhat higher, but within errors, if M and R in the spectral model are restricted to the more compact BSk21 EOS.

The goodness of the fit is illustrated by the χ^2 value obtained for the 1653 spectral energy bins as shown in the last column in Table 1. One traditionally uses the reduced χ^2 in order to quantify the quality of the fit. To this end it is necessary to know the number of degrees of freedom (d.o.f.), which is in fact not trivial for non-linear models, especially for the models with hierarchical priors as we have here (e.g., Andrae, Schulze-Hartung & Melchior 2010). Our estimate for the degrees of freedom in Table 1 is actually a lower limit. Therefore, the reduced $\chi^2/\text{d.o.f.}$ is about 1 for all considered models, indicating acceptable fits.

The large values for the cooling slope s ($s > 0$ at more than the 6σ level, see Table 1) require enhanced cooling of the CasA NS, which we attribute to the presence of CPF neutrino emission.

3 COOPER PAIRING NEUTRINO EMISSION

3.1 Cooling of superfluid NSs

Let us outline the cooling theory of superfluid NSs (minimal cooling; Gusakov et al. 2004; Page et al. 2004). In general, an initially hot neutron star cools via two cooling channels – neutrino emission from the NS bulk and photon emission from the surface (e.g., Yakovlev & Pethick 2004). The latter becomes important at late stages of the NS cooling ($t \gtrsim 10^5$ yr), while the neutrino emission dominates earlier. Initially, extremely strong neutrino emission introduces large temperature gradients inside the star. However, while the NS cools and neutrino emissivity becomes less powerful, the large thermal conductivity washes these gradients out. Therefore, at $t > 10 - 100$ yr (e.g., Nomoto & Tsuruta 1981; Richardson et al. 1982; Gnedin, Yakovlev & Potekhin 2001; Shternin & Yakovlev 2008), the NS becomes isothermal inside, except for the thin ‘heat blanketing’ outer envelope. Because of the effects of General Relativity, the isothermality means that it is the redshifted temperature $\tilde{T} = T \exp(\Phi)$, where Φ is the metric function (e.g., Thorne 1966), that is spatially constant. At this neutrino cooling stage, the equation that describes the cooling of the star becomes extremely simple:

$$\frac{d\tilde{T}}{dt} = -\ell(\tilde{T}) = -\frac{L_\nu^\infty(\tilde{T})}{C(\tilde{T})}, \quad (1)$$

where $C(\tilde{T})$ is the integrated heat capacity of the star and $L_\nu^\infty(\tilde{T})$ is the integrated neutrino luminosity (the superscript ∞ indicates that the GR effects are taken into account). There are many processes

that contribute to the neutrino emission from NS interiors (see, e.g., Yakovlev et al. 2001; Potekhin, Pons & Page 2015; Schmitt & Shternin 2018, for reviews). In a non-superfluid NS, the so-called slow cooling processes, including the modified Urca and nucleon bremsstrahlung, have $L_\nu^\infty(\tilde{T}) \propto \tilde{T}^8$. Since $C(\tilde{T}) \propto \tilde{T}$, one obtains $\ell(\tilde{T}) \propto \tilde{T}^7$, and the solution of equation (1) for the initial condition $\tilde{T}_0 \gg \tilde{T}$ results in the standard neutron star cooling law $\tilde{T}(t) \propto t^{-1/6}$.

We adopt a standard assumption (Page et al. 2011; Shternin et al. 2011) that the rapid cooling of the CasA NS is explained by a splash of neutrino emission at the onset of the neutron triplet superfluidity. It occurs at the moment $t = t_C$ when the star cools down to the maximal critical temperature \tilde{T}_{Cnmax} in the core. Shortly after, the CPF neutrino emission becomes the main cooling process. At the same time, neutron pairing suppresses the previous slow cooling processes. At this time,

$$\ell \approx \ell_{CPF} \equiv \frac{L_{CPF}^\infty}{C_\ell + C_{nSF}}, \quad (2)$$

where L_{CPF}^∞ is the integrated luminosity of the CPF emission. The heat capacity in the denominator includes the contributions from leptons, C_ℓ , and neutrons, C_{nSF} , with the latter accounting for the pairing modifications. Notice that the standard approach to the CasA NS cooling assumes that most of the protons in the core are in the paired state, thus providing negligible contribution to the heat capacity (Page et al. 2011; Shternin et al. 2011). Knowing ℓ_{CPF} allows one to calculate the thermal evolution of the superfluid NS. The initial segment of the cooling curve (at $\tilde{T}_{Cnmax} \gtrsim \tilde{T} \gtrsim 0.6\tilde{T}_{Cnmax}$) can be described by universal self-similar solutions (Shternin & Yakovlev 2015). When superfluidity becomes well-developed (at $\tilde{T} \lesssim 0.1\tilde{T}_{Cnmax}$), the cooling resembles the slow cooling with $\ell_{CPF} \propto \tilde{T}^n$ and $n \approx 7$ (Gusakov et al. 2004) [the power exponent n can differ from $n = 7$ depending on the functional form of the wings of $T_{Cn}(\rho)$].

In order to connect the cooling solutions to observations, one needs to relate the internal temperature \tilde{T} and the surface temperature T_s . The main temperature gradient is located in the heat blanketing envelope. The dependence of T_s on the temperature $T_b = \tilde{T}/\sqrt{1-x_g}$ [here $x_g = 2GM/(Rc^2)$ is the compactness parameter, G is the gravitational constant and c is the speed of light] at the bottom of this envelope depends on its composition, the surface gravity (hence M and R), and possibly on other factors such as the magnetic field strength and geometry. Since we assume a carbon atmosphere for the CasA NS, the outer layers of the envelope cannot contain lighter elements (such as H or He) because of strong gravitational stratification. On the other hand, the amount of carbon in the envelope that is required to form the carbon atmosphere is so small that it may not affect the $T_s(T_b)$ relation; in this case, the latter can be approximated by the relation for the iron envelope. Here we adopt the expressions for the iron envelopes given by Potekhin, Chabrier & Yakovlev (1997) and C-Fe envelopes from Beznogov, Potekhin & Yakovlev (2016). Notice that the composition of the envelope, and hence the $T_s(T_b)$ relation, can change in time due to the diffusive nuclear burning of light elements (Chang & Bildsten 2003; Wijngaarden et al. 2019, 2020). We also note that according to the previous analysis (Shternin & Yakovlev 2015), a large amount of carbon in the envelope cannot be reconciled with the CasA NS observations.

For a wide range of models, the $T_s(T_b)$ relation obeys a simple scaling property $T_s \propto T_b^\beta$ with $\beta \approx 0.53$. We adopt this relation below. The uncertainty introduced by the difference of more accurate values of β is much smaller than the other sources of uncertainties in our analysis. Notice for completeness, that such a simple scaling

Table 2. Parameters derived from the spectral fit. Uncertainties correspond to the 68 per cent highest posterior density credible intervals. See Table 1 for the definitions of the different models.

Model	\tilde{T}_d 10 ⁸ K	x_g	x_ρ	ℓ_d MK yr ⁻¹	qF_d
1	2.97 ^{+0.25} _{-0.40}	0.27 ^{+0.07} _{-0.06}	2.3 ^{+2.0} _{-1.5}	1.02 ^{+0.17} _{-0.19}	0.68 ^{+0.18} _{-0.28}
2	2.83 ^{+0.29} _{-0.28}	0.30 ^{+0.06} _{-0.06}	2.7 ^{+1.6} _{-1.6}	0.88 ^{+0.13} _{-0.14}	0.59 ^{+0.21} _{-0.20}
3	2.60 ^{+0.16} _{-0.13}	0.37 ^{+0.04} _{-0.06}	5.6 ^{+0.6} _{-0.9}	0.97 ^{+0.17} _{-0.15}	0.84 ^{+0.21} _{-0.15}
4	2.57 ^{+0.14} _{-0.13}	0.38 ^{+0.03} _{-0.06}	5.8 ^{+0.5} _{-0.9}	0.86 ^{+0.12} _{-0.12}	0.77 ^{+0.18} _{-0.13}

relation breaks at low temperatures (see, e.g., Potekhin et al. 2003), irrelevant for the CasA NS study.

Now the observed slope of the cooling curve can be directly connected to the neutrino cooling rate in equation (1),

$$s = -\frac{d \ln T_s}{d \ln t} \approx -\beta \frac{d \ln \tilde{T}}{d \ln t}. \quad (3)$$

Clearly, the slow cooling ($\tilde{T} \propto t^{-1/6}$) predicts $s_{slow} \approx 1/12$, much less than observed (see Table 1). In contrast, the evolution of the cooling slope when CPF emission is dominant has a bell-like shape, with s reaching some maximal value s_{max} (e.g., Shternin & Yakovlev 2015).

From equations (1) and (3) we straightforwardly obtain the ‘detected’ cooling rate ℓ_d ,

$$\ell_d = \frac{s_d}{\beta} \frac{\tilde{T}(T_{sd})}{t_d}, \quad (4)$$

provided the envelope model is chosen. In equation (4), s_d , t_d and T_{sd} stand for the detected values of the cooling slope, age and surface temperature, respectively⁵. Accordingly, $\tilde{T}_d \equiv \tilde{T}(T_{sd})$. For a pure iron heat-insulating envelope (more exactly, for a small mass of light elements, $\Delta M < 10^{-16} M_\odot$), the results are shown in Table 2.⁶ The standard cooling candle (Yakovlev et al. 2011) at $t = 330$ yr would have a much smaller $\ell_{SC} = 0.16 \pm 0.03$ MK yr⁻¹ (this value is marginalized over the $M - R$ distribution for spectral model 1).

3.2 Analysis of the Cooper pair emission

The CPF neutrino emissivity can be written as (e.g., Yakovlev et al. 2001; Schmitt & Shternin 2018)

$$Q_{CPF} = q Q_{CPF0} T^7 \mathcal{F}(v), \quad (5)$$

where

$$Q_{CPF0} = 1.17 \times 10^{-42} \left(\frac{m_n^*}{m_N} \right) \left(\frac{p_{Fn}}{m_N c} \right) N_\nu a_n \text{ erg cm}^{-3} \text{ s}^{-1} \text{ K}^{-7}, \quad (6)$$

$N_\nu = 3$ is the number of neutrino flavors, m_n^* is the neutron effective mass on the Fermi surface, p_{Fn} is the neutron Fermi momentum, and m_N is the bare nucleon mass. $a_n = g_V^2 + 2g_A^2 = 4.17$ is a numerical constant which encapsulates contributions from the vector part of the weak current (with the coupling constant $g_V \approx 1$) and the axial-vector part of the weak current (with the coupling

⁵ From now on, we use the d subscript for the detected quantities in order to distinguish them from general variables entering various functional laws.

⁶ The quantities x_ρ and qF_d in Table 2 are defined in the following sections.

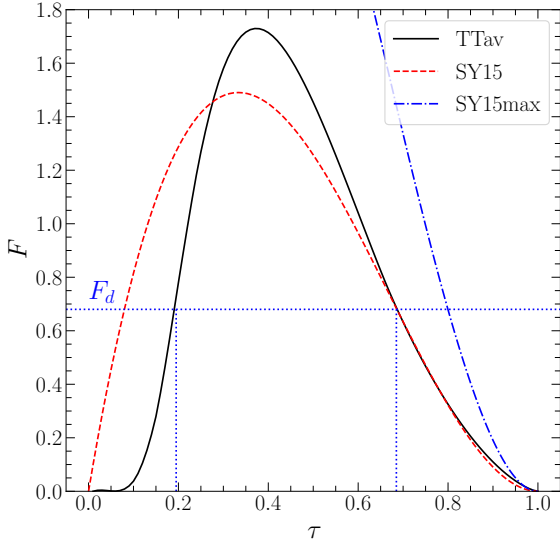


Figure 2. The function $F(\tau)$ for the ‘TTav’ superfluidity profile (Takatsuka & Tamagaki 2004), BSk21 EOS and a NS mass of $M = 1.4 M_\odot$ (solid line). The blue dotted horizontal line shows some detected value F_d and the two vertical dotted lines indicate two possible solutions for τ_d at this F_d and this $F(\tau)$ profile. The dashed line shows the self-similar profile equation (13) normalized by the maximum of $\mu = \tau^6 F(\tau)$ for the ‘TTav’ profile. The dash-dotted line gives the highest possible self-similar profile that corresponds to $\mu_{\max} = 0.18$.

constant $g_A \approx 1.26$). $\mathcal{F}(v)$ in equation (5) is an auxiliary function which depends on the dimensionless gap parameter $v = \Delta_0/(k_B T)$, where k_B and Δ_0 are the Boltzmann constant and neutron triplet gap amplitude, respectively. The analytical fit for the function $\mathcal{F}(v)$ can be found, e.g., in Yakovlev et al. (2001) [see case B in their equation (241)].

The phenomenological factor q in equation (5) takes into account many-body corrections, the most prominent of which is related to the response of the superfluid condensate. It was realized that, due to the requirement of vector current conservation, the interaction in the vector channel needs to be renormalized (Kundu & Reddy 2004; Leinson & Pérez 2006). As a consequence, the CPF emission in the singlet (1S_0) phase of the neutron pairing is strongly suppressed. This was suggested by Leinson & Pérez (2006) and confirmed later by many authors (see Leinson 2018, for a review). Accordingly, Page et al. (2009) proposed a phenomenological correction to equation (5) which corresponds to the triplet pairing neutron superfluidity completely suppressing the vector channel, so that $q = 2g_A^2/a_n = 0.76$. This correction was used in the CasA NS cooling scenarios (Page et al. 2011; Shternin et al. 2011; Wijngaarden et al. 2019). However, taking into account the axial-vector response of the order parameter in the triplet case, Leinson (2010) found that the CPF emission is further suppressed by an additional factor of 4 (in the non-relativistic limit), giving $q = g_A^2/(2g_V^2 + 4g_A^2) \approx 0.19$. Anyhow, one can assume that the CPF emission is suppressed, giving $q < 1$. Notice that the small value of q calculated by Leinson (2010) makes the successful explanation of the CasA NS cooling observations challenging (Shternin et al. 2011; Shternin & Yakovlev 2015; Potekhin & Chabrier 2018).

The total integrated CPF neutrino luminosity (redshifted for a distant observer) is

$$L_{\text{CPF}}^\infty = \int_0^{R_{\text{core}}} Q_{\text{CPF}} \frac{\exp(2\Phi) 4\pi r^2 dr}{\sqrt{1-x_g}}, \quad (7)$$

where R_{core} is the radius of the NS core. It is hardly possible to construct fully model-independent expressions for L_{CPF}^∞ since it depends at least on the unknown shape of $T_{Cn}(\rho)$ in the NS core. Nevertheless, it is possible to extract the main M , R and EOS dependence following the approach of Ofengeim et al. (2017). To this end, it is instructive to separate the temperature and profile-independent part of equation (5) by introducing the quantity

$$\Lambda_{\text{CPF}} = \int_0^{R_{\text{core}}} Q_{\text{CPF0}} \frac{\exp(-5\Phi) 4\pi r^2 dr}{\sqrt{1-x_g}}. \quad (8)$$

The term $\exp(-5\Phi)$ results from the combination of the seventh power of $T = \tilde{T} \exp(-\Phi)$ in equation (5) and the metric factor in equation (7) [remember that \tilde{T} is assumed to be constant through the core and thus can be taken out of the integral in (7)]. This separation is convenient, as Λ_{CPF} can be fitted by expressions similar to those used by Ofengeim et al. (2017). Assuming that m_n^* is independent of density (see Section 5), we obtain

$$\Lambda_{\text{CPF}} = 1.17 \times 10^{-24} \left(\frac{m_n^*}{m_N} \right) \left(\frac{R}{10 \text{ km}} \right)^3 J_{1,5}(M, R) \text{ erg s}^{-1} \text{ K}^{-7}, \quad (9)$$

where the function $J_{1,5}$ is defined in Ofengeim et al. (2017) and detailed in Appendix C.

The heat capacity modification due to neutron superfluidity also depends on $T_{Cn}(\rho)$ and is not universal. With the same lines of reasoning as for the CPF neutrino emissivity above, we normalise the heat capacity to the total heat capacity of a NS with completely superfluid protons and normal neutrons, $C_\ell + C_n$. The universal expression for these contributions is $C_\ell + C_n = \Sigma_{n\ell}(M, R)\tilde{T}$, where

$$\Sigma_{n\ell} = 1.12 \times 10^{29} \left(\frac{R}{10 \text{ km}} \right)^3 J_{1,1}(M, R) \text{ erg K}^{-2}, \quad (10)$$

and $J_{1,1}$ is also specified in Appendix C [cf. equations (20) and (21) in Ofengeim et al. (2017); case ‘ $n\ell$ ’ in Table IV there]. Unless indicated otherwise, we set $m_n^* = 0.7m_N$.

Now the superfluid cooling function can be written as

$$\ell_{\text{CPF}} = \frac{L_{\text{CPF}}}{C_\ell + C_{nSF}} = q \frac{\Lambda_{\text{CPF}}}{\Sigma_{n\ell}} \tilde{T}^6 F(\tau), \quad (11)$$

where

$$qF(\tau) = \frac{L_{\text{CPF}}/(C_\ell + C_{nSF})}{\Lambda_{\text{CPF}}\tilde{T}^6/\Sigma_{n\ell}}, \quad (12)$$

and $\tau = \tilde{T}/\tilde{T}_{Cn\max}$. Thus, $F(\tau)$ is an effective average of the $\mathcal{F}(v)$ over the stellar model for a given critical temperature profile. Notice that the contributions to heat capacities in the numerator and denominator of equation (12) are different. This is a result of superfluid modification of the neutron contribution to the heat capacity.

The function $F(\tau)$ in equation (12) depends on the dimensionless redshifted critical temperature profile, $\tilde{T}_{Cn}(\rho)/\tilde{T}_{Cn\max}$, in a given NS and on the NS EOS. We stress that $F(\tau)$ does not depend on the value of $\tilde{T}_{Cn\max}$ for the specified pairing model. Typically, the function $F(\tau)$ has a bell-like shape even if the critical temperature profile $T_{Cn}(\rho)$ is not bell-like. An illustrative $F(\tau)$ is shown in

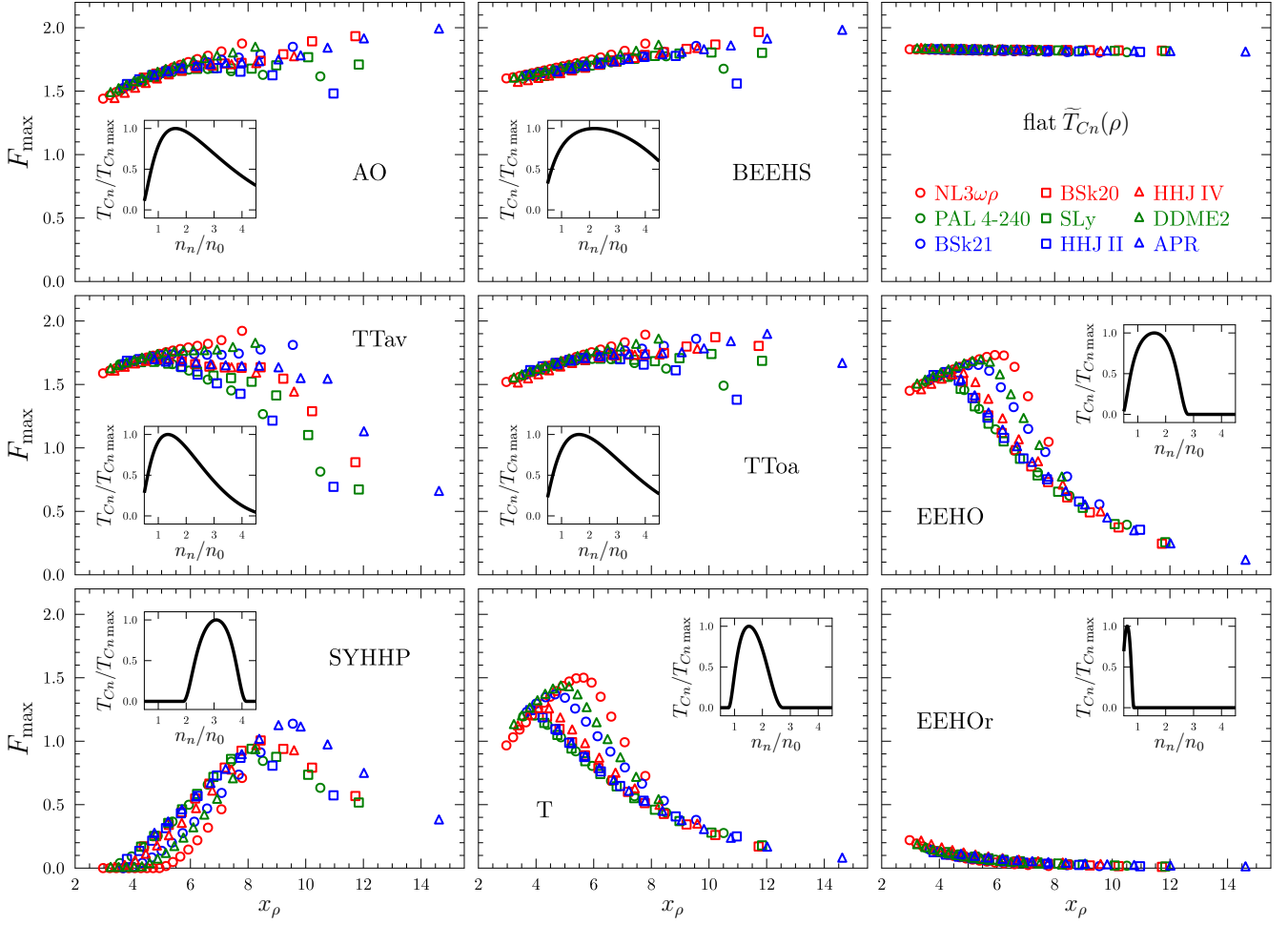


Figure 3. Maximum values of the function $F(\tau)$ [see equation (12)] versus dimensionless mean density $x_\rho = M/(R^3 \rho_0)$ of the neutron star. Each panel corresponds to one model of the critical temperature profile: the upper right corner corresponds to flat $\tilde{T}_{Cn}(\rho)$; in other cases the $T_{Cn}(n_n)$ profiles, where n_n is the neutron number density, are taken from Ho et al. (2015) (abbreviations AO, BEEHS, etc., are the same as in that paper) and shown in insets (with n_n normalised by $n_0 = 0.16 \text{ fm}^{-3}$). Each symbol corresponds to a NS model with a given mass and EOS.

Fig. 2 by the solid line. Here we use the neutron superfluidity model from Takatsuka & Tamagaki (2004), noted as ‘TTav’ in Ho et al. (2015). The function $F(\tau)$ reaches a maximal value $F_{\max} = 1.73$ at $\tau_F = 0.37$; these values are typical, although they vary from one profile to another. As we will show in Section 4.1, F_{\max} is important in applications. Clearly, it depends on the volume of superfluid region present inside the star (in other words, on the position of the maximum of $\tilde{T}_{Cn}(\rho)$ with respect to the central density). We calculated $F(\tau)$ for many combinations of the EOSs, superfluidity models and NS models ranging from $M = 1 M_\odot$ to the maximal mass for a given EOS. In Fig. 3, we show F_{\max} for 9 superfluidity profiles. One of them assumes the flat $\tilde{T}_{Cn}(\rho)$ dependence; the other profiles are the same as in Ho et al. (2015). Each panel corresponds to one profile (as indicated in the plot) and 9 EOSs (the same as used in Ofengeim et al. 2017). Each EOS is shown by a different symbol, as indicated in the legend in the top right panel. The quantity F_{\max} is plotted as a function of the dimensionless mean density $x_\rho = M/(R^3 \rho_0)$, where $\rho_0 = 2.8 \times 10^{14} \text{ g cm}^{-3}$ is the nuclear saturation density. The parameter F_{\max} increases with x_ρ because the central density moves towards the peak of $\tilde{T}_{Cn}(\rho)$. If the superfluidity is mainly localised in the outer core, as in the case

of the ‘T’ profile (Fig. 3), F_{\max} reaches a maximum and decreases in more massive stars, since a large part of the inner core does not contain paired neutrons. For most of the models investigated here, the value of τ where F reaches a maximum, τ_F , lies in the range 0.2–0.5.

The neutrino cooling rate due to Cooper pairing, ℓ_{CPF} , is proportional to $\mu = \tau^6 F(\tau)$ [see equation (2)]. The quantities μ and ℓ_{CPF} reach maxima at much larger $\tau_\mu \approx 0.8$ (e.g., Gusakov et al. 2004). Around this value of τ , NS cooling due to CPF emission can be well-described by the self-similar analytical solutions suggested by Shternin & Yakovlev (2015). These solutions approximate $F(\tau)$ by a simple formula

$$F(\tau) \approx F_{\text{SY}}(\tau) \equiv 117.6 \mu_{\max} \tau (1 - \tau)^2, \quad (13)$$

where μ_{\max} is the maximal value of μ for a given profile. Then the neutrino cooling rate in equation (1) becomes

$$\ell(\tau) = \ell_0 \tau^6 \left[\tau + 117.6 \delta \tau (1 - \tau)^2 \Theta(1 - \tau) \right], \quad (14)$$

where ℓ_0 is the level of neutrino luminosity at $\tau = 1$ (i.e. before superfluidity onset). The first term in brackets accounts for slow

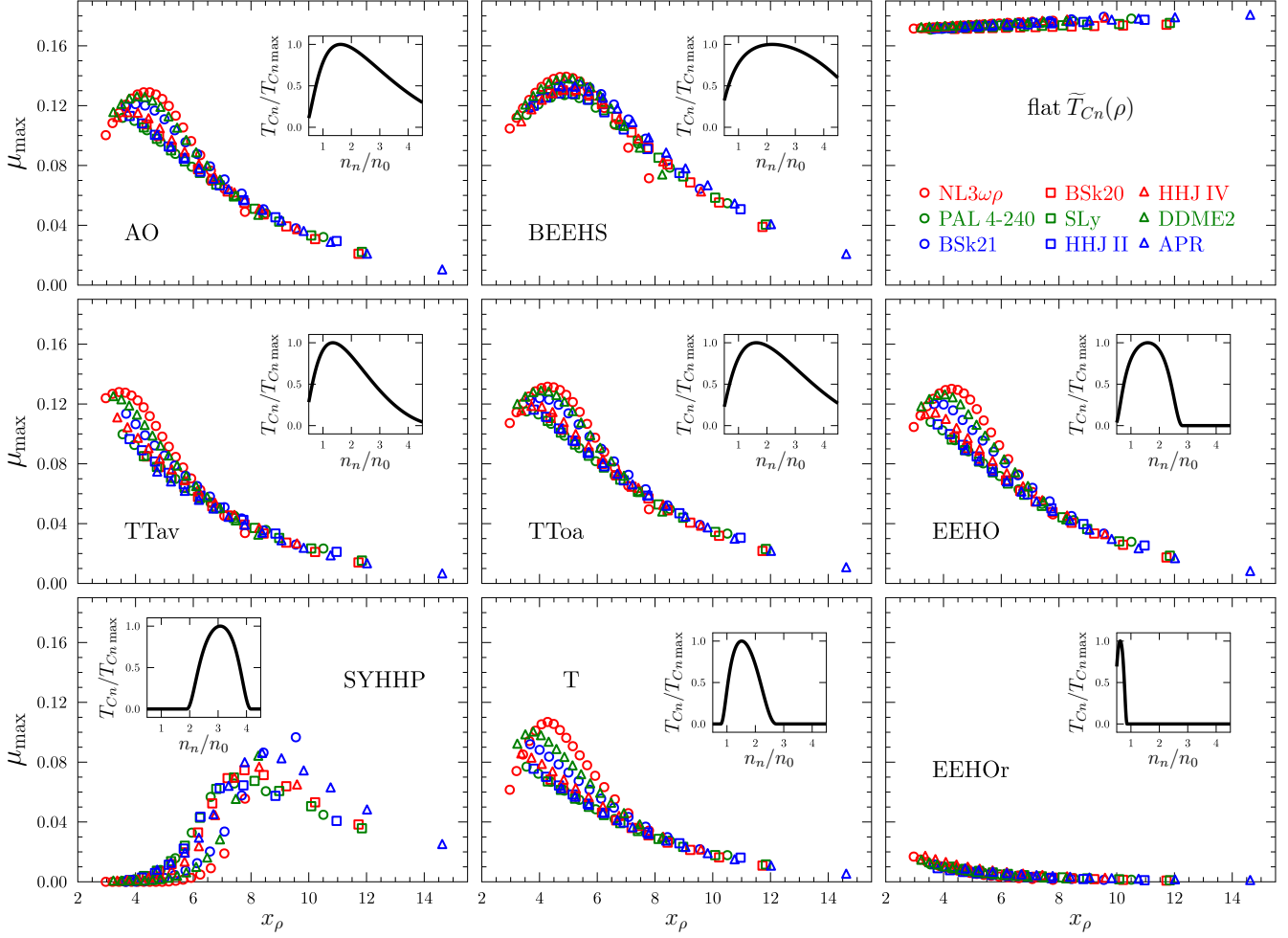


Figure 4. The same as in Fig. 3 but for the maximal value $\mu_{\max} = \max[\tau^6 F(\tau)]$.

cooling, and the step function $\Theta(1 - \tau)$ in the second term ensures that the CPF emission operates at $\tau < 1$. The power of the CPF emission in self-similar solutions is regulated by the parameter δ , which is the ratio of the maximum of ℓ_{CPF} and the neutrino cooling rate ℓ_0 (Shternin & Yakovlev 2015):

$$\delta = \frac{\max \ell_{\text{CPF}}}{\ell_0} = \frac{q \Lambda_{\text{CPF}} \tilde{T}_{Cn\max}^6}{\Sigma_{nt} \ell_0} \mu_{\max}. \quad (15)$$

For a given δ , the self-similar solution results in the bell-shaped dependence of the cooling slope, $s(\tau)$, with a maximum near $\tau_\mu \approx 0.8$. The maximal value s_{\max} and the whole bell-like curve $s(\tau)$ increase with δ (Shternin & Yakovlev 2015). If one assumes an initial slow cooling mechanism ($n = 7$), then $\ell_0 = Q_0 \tilde{T}_{Cn\max}^7$, where Q_0 is the temperature-independent prefactor. This results in $\delta \propto \tilde{T}_{Cn\max}^{-1}$ scaling for a given EOS and initial neutrino emission model (Gusakov et al. 2005; Shternin & Yakovlev 2015).

The self-similar solutions are valid at $\tau \gtrsim 0.6$ (Shternin & Yakovlev 2015; Gusakov et al. 2004). This is illustrated by the red dashed line in Fig. 2, which represents the approximate expression (13) calculated using μ_{\max} for the exact ‘TTav’ profile (shown by the solid line). One sees an impressive agreement between the actual $F(\tau)$ and the simple analytical expression $\tau \gtrsim 0.6$, while at $\tau < 0.6$ the curves diverge. In other words, all the different $F(\tau)$ for different

superfluidity profiles, different EOSs and so on, have similar shapes at $\tau > 0.6$ and behave differently at $\tau < 0.6$.

The maximal value of the cooling rate, μ_{\max} , demonstrates much less scatter than F_{\max} , as shown in Fig. 4 which has a similar design as Fig. 3. One sees a relatively modest dependence of μ_{\max} on the EOS for a given superfluidity profile. Moreover, our investigations show that there exists a universal upper limit for μ_{\max} that is reached for the unrealistic flat redshifted critical temperature profile $\tilde{T}_{Cn}(\rho) = \text{const}$. The dependence $\mu_{\max}^{\text{flat}}(x_\rho)$ is shown in the top-right panel of Fig. 4 for the EOSs investigated here. Clearly, $\mu_{\max}^{\text{flat}} \approx 0.18$, with slightly lower values at the lowest x_ρ . Notice that for F_{\max} , the flat $\tilde{T}_{Cn}(\rho)$ profile does not provide the upper limit; by choosing a peculiar critical temperature profile, one can overcome (although not dramatically) the maximal $F(\tau)$ reached by the flat profile. This is a consequence of the fact that the realistic profiles typically have bell-like shapes.

The existence of upper limits for F_{\max} and μ_{\max} provides constraints on superfluidity models that can successfully explain the observations of the CasA NS cooling.

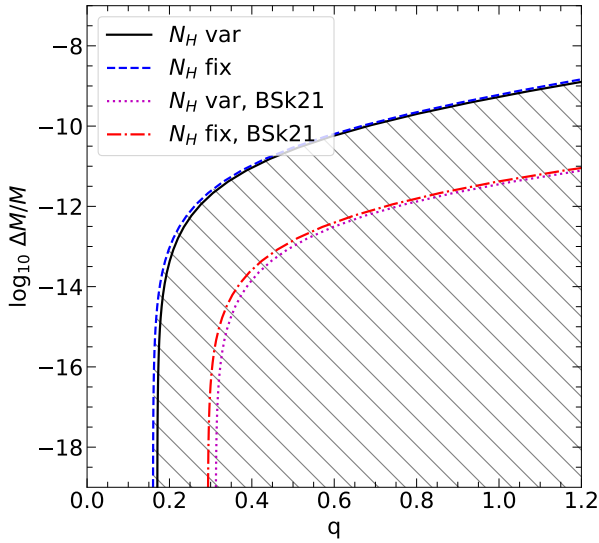


Figure 5. 95 per cent credibility lower limit on possible values of q based on the condition $F_d < 2$ for different amounts of light elements in the heat blanketing envelope. Different linestyles correspond to different spectral models as indicated in the legend. The allowed parameter region is to the right of the corresponding curve (hatched region for model 1).

4 APPLICATION TO CASA NS COOLING

4.1 Analysis based on F_d

We start from the analysis based on the direct measurement of the cooling slope and the surface (internal) temperature. If one neglects the slow mechanism of neutrino emission and assumes that the current cooling is mainly regulated by the CPF mechanism, from equations (1), (3) and (11) one immediately obtains the ‘detected’ value of F

$$qF_d = \frac{s_d \Sigma_{n\ell}}{\beta t_d \Lambda_{\text{CPF}} \tilde{T}_d^5}, \quad (16)$$

where t_d is the current age of the star (assumed to be 330 yr). The values of qF_d obtained from observations are given in Table 2 (for the iron heat blanketing envelope) and are compatible for all four models under consideration.

An immediate constraint follows from the requirement for F_d to be smaller than F_{max} . According to Fig. 3, for a particular superfluidity model, this is possible only for a range of x_ρ , i.e., for a range of NS masses. Moreover, some superfluidity models, like EEHOr, cannot be reconciled with observations since they give too low values of F for all ranges of parameters. Clearly, there is a global upper limit, $F_{\text{max}} < 2$. Observing $F_d > 2$ makes explanation of the cooling of CasA NS by superfluidity models extremely problematic.

According to equation (16), the condition $F_d < F_{\text{max}} < 2$ restricts the possible range of q . For the iron heat blanketing envelope, from this restriction one obtains $q > 0.17$ ($q > 0.16$) for the variable (fixed) N_H model at 95 per cent credibility level for the general models (not restricted to the BSk21 EOS). A possible limit on q depends strongly on the $T_s(T_b)$ relation (on a model of heat blanketing envelope) because of the strong \tilde{T}_d^5 dependence in equation (16). For instance, taking the classical heat blanketing rela-

tion of Gudmundsson, Pethick & Epstein (1983), one gets a slightly smaller \tilde{T}_d , but a factor of 1.5 larger F_d , resulting in stronger restrictions on q . Accordingly, light elements in the heat blanketing envelope make it more transparent, thus decreasing \tilde{T}_d for a given T_{sd} . This increases F_d , shrinking the available parameter space for the CPF process.

In Fig. 5, we plot the 95 per cent lower limit on q as described above for different values of $\Delta M/M$ of carbon in the heat blanketing envelope for four models described in Section 2. Low amounts of carbon ($\Delta M/M < 10^{-14}$) do not significantly affect the inference of F_d and hence of q_{min} . On the other hand, at $\Delta M/M \gtrsim 10^{-10}$, the lowest possible q , according to our results, is already more than one for all considered models. Therefore a large amount of light elements in the envelope is problematic for the superfluid explanation of the CasA NS cooling (Shternin et al. 2011; Shternin & Yakovlev 2015).

This is in line with the discussion in Wijngaarden et al. (2019) who showed that, to preserve/obtain the carbon atmosphere for a star of CasA age, the accretion rate of the fall-back material should be less than some $10^{-20} M_\odot \text{ yr}^{-1}$, resulting in $\Delta M/M \lesssim 3 \times 10^{-18}$. Larger accretion rates, that will result in a large amount of light elements in the envelope, would not allow for the lightest elements such as H and He to burn into carbon completely and thus would prevent the formation of the carbon atmosphere. Therefore in further analysis, we will assume a negligible amount of light elements in the envelope which does not influence \tilde{T} .

4.2 Constraining superfluid critical temperature

Let us assume that we know the EOS, superfluidity profile and other microphysical input and want to constrain the superfluid transition temperature. For a given dimensionless profile $F(\tau)$, there exists a maximal possible value of the cooling slope s_d^{max} that can be reached at the observed \tilde{T} . This maximal value corresponds to the maximum of $F(\tau)$, i.e. $\tau \approx \tau_F$ [see equation (16)]. If $s_d > s_d^{\text{max}}$, the successful explanation of the observations is impossible and one needs to select another superfluidity profile $F(\tau)$ or increase q . If $s_d < s_d^{\text{max}}$, there are two solutions $F(\tau_d) = F_d$ (Shternin & Yakovlev 2015), before and after the maximum of F (see Fig. 2). Since neither $F(\tau)$ nor q is known, it is impossible to obtain τ_d and hence $T_{C\text{max}}$ from these two solutions directly. Nevertheless, it is possible to constrain τ_d from general restrictions on the cooling models.

4.2.1 Upper limit on τ_d

Let us consider first a large τ . In this case the self-similar solutions work well. As shown in Section 3.2, the function $F(\tau)$ for each superfluidity profile at $\tau > 0.6$ can be characterized just by the corresponding value of μ_{max} [see equation (13)]. The global restriction $\mu_{\text{max}} < 0.18$ suggests that the actual (τ_d, F_d) pair needs to reside below the maximal self-similar curve shown with the dash-dotted line in Fig. 2. According to equation (13), this limit is set by the inequality

$$F_d \leq F_{\text{SYmax}}(\tau_d) = 21.2 \tau_d (1 - \tau_d)^2, \quad \text{at } \tau_d > 0.6. \quad (17)$$

This equation constrains τ_d from above for a given F_d independently of a particular superfluidity model. In Fig. 2, it is given by the intersection of the horizontal dotted line with the dash-dotted curve [when the inequality in equation (17) turns to equality]. In the case shown in Fig. 2, it is about 0.8 (for model 1 and $q = 1$). Smaller

values of the parameter q increase F_d and shift this maximal τ_d to lower values.

The error propagation from measured uncertainties in F_d to uncertainties in τ_d via equation (17) is not completely trivial, and we save the detailed incorporation of this limit to Section 4.3. Instead, we notice that equation (16) actually allows us to set a lower limit on the absolute value of the maximal critical temperature $\tilde{T}_{Cn\max}$ instead of τ_d . Indeed, multiplying equation (16) by $\tilde{T}_{Cn\max}^5$ and rearranging terms, one obtains

$$q^{1/5} \tilde{T}_{Cn\max} = \left[\frac{s_d \Sigma_{n\ell}}{\beta t_d \Lambda_{\text{CPF}} F_d \tau_d^5} \right]^{1/5} > 1.33 \left[\frac{s_d \Sigma_{n\ell}}{\beta t_d \Lambda_{\text{CPF}}} \right]^{1/5}, \quad (18)$$

where the last inequality results from the restriction $\tau_d^5 F_d < \max\{\tau^5 F(\tau)\} < 1.3\mu_{\max} < 0.23$. Here we use the fact that the maximum of $\tau^5 F(\tau)$ is reached at the ‘self-similar’ part of $F(\tau)$ (at $\tau = \arg\max \tau^5 F(\tau) \equiv \tau_5 \approx 0.75$); thus it is given by $F_{\text{SY}\max}(\tau_5) = 0.23$ [see equation (17)]. The advantage of equation (18) is that it gives a direct constraint on $\tilde{T}_{Cn\max}$ and does not depend on the heat blanketing envelope model (except for a weak dependence via the parameter β). Therefore, this limit is quite robust and has a simple scaling with q . The corresponding upper limit on τ_d can be obtained from equation (18) by dividing by \tilde{T}_d . In contrast to a lower limit on $\tilde{T}_{Cn\max}$, it depends on the envelope model. We give the boundaries of the 90 per cent one-sided credible intervals for the limiting values $q^{1/5} \tilde{T}_{Cn\max}^{\text{low}}$ and $q^{-1/5} \tau_d^{\text{up}}$ in Table 3.⁷

4.2.2 Lower limit on τ_d

Now consider the case of a small τ_d . This possibility requires a large contrast between the initial slow cooling and the CPF mechanism (the neutrino splash was long ago, but the cooling is still fast). Indeed, due to the bell-like shape of the cooling slope dependence, the solution of the equation $s(\tau_d, \delta) = s_d$ with $\tau_d < \tau_\mu \approx 0.8$ requires an increase in δ if τ_d is decreasing [see equation (15) and Shternin & Yakovlev (2015)]. By definition, lowering τ_d for a given \tilde{T}_d means increasing $\tilde{T}_{Cn\max}$ [recall that $\delta \propto \tilde{T}_{Cn\max}^{-1}$; see discussion below equation (15)]. Therefore lowering τ_d for a fixed initial cooling rate (i.e., fixed Q_0) decreases δ . These two factors combined together require a much smaller initial cooling rate Q_0 when lowering τ_d . It is instructive to express the initial slow cooling rate in terms of the standard neutrino candle instead of Q_0 (Yakovlev et al. 2011; Shternin & Yakovlev 2015; Ofengeim & Yakovlev 2017a). This is done by introducing a parameter $f_{\ell 0} = \ell_0(\tilde{T})/\ell_{\text{SC}}(\tilde{T})$ (assuming that the standard candle and initial slow cooling have the same temperature dependencies). Let $\tilde{T}_{\text{SC}}(t)$ be the standard candle cooling curve (Yakovlev et al. 2011),

$$\tilde{T}_{\text{SC}}(t) = 3.45 \times 10^8 (1-x_g) \left[1 + 0.12 \left(\frac{R}{10 \text{ km}} \right)^2 \right] \left(\frac{t}{330 \text{ yr}} \right)^{-1/6} \text{ K}. \quad (19)$$

Then

$$f_{\ell 0} = \tau_d^6 \frac{t_d}{t_C} \left(\frac{\tilde{T}_{\text{SC}}(t_d)}{\tilde{T}_d} \right)^6. \quad (20)$$

The value of $f_{\ell 0}$ (or Q_0) cannot be arbitrarily small. The weakest possible neutrino emission at the initial cooling stage in our model

occurs when the protons are fully paired and only the neutron-neutron (and much weaker lepton) bremsstrahlung remains as a neutrino-generation process. The neutron-neutron bremsstrahlung is unavoidable, since the neutron pairing has not yet started at the initial stage. Therefore it provides a natural lower limit for the neutrino cooling rate, $f_{\ell 0} > f_{\ell nn}$, where $f_{\ell nn}$ is nn bremsstrahlung rate relative to the standard neutrino candle. The model-independent (again with respect to EOS; see discussion in Section 5) analytical expression for the integrated nn bremsstrahlung neutrino luminosity was constructed by Ofengeim et al. (2017). This expression is based on the Friman & Maxwell (1979) calculations in the one-pion exchange model of the strong interaction. The approximation of Ofengeim et al. (2017) proved to be valid for a wide range of EOS of dense matter.

In order to apply the constraint $f_{\ell 0} > f_{\ell nn}$ we need to calculate $f_{\ell 0}$. Equation (20) shows that to this end it is necessary to calculate t_C as a function of τ_d , i.e. to follow the cooling curve into the past. In principle, we cannot do it in a model-independent way for very low values of τ , since at $\tau < 0.6$ each superfluidity profile results in its own $F(\tau)$ shape and hence in a unique cooling curve. However, the main dependence on τ_d in equation (20) for not very low τ_d is in the sixth-power factor τ_d^6 and not in the cooling curve $t_d/t_C(\tau_d)$. Thus some imprecision in t_C estimates is possible. We decided to use self-similar solutions from Shternin & Yakovlev (2015) to calculate t/t_C and, as a consequence, $f_{\ell 0}$ even for $\tau_d < 0.6$. Among the realistic models we considered, this introduces less than 20 per cent error in t_C down to $\tau_d = 0.25$. This is acceptable, since *a posteriori* such a low τ_d requires too small $f_{\ell 0}$ for the CasA NS.

From equations (1), (3) and (14), the cooling slope for the self-similar solutions can be written as

$$s_d = \frac{\beta}{6} \tau_d^6 \frac{t_d}{t_C} \left(1 + 117.6 \delta (1 - \tau_d)^2 \right). \quad (21)$$

Combining this equation with equation (20) allows us to express the parameter δ for a given $f_{\ell 0}$ and τ_d as

$$\delta(\tau_d) = 0.0085 \left[\frac{6s_d}{\beta f_{\ell 0}} \left(\frac{\tilde{T}_{\text{SC}}(t_d)}{\tilde{T}_d} \right)^6 - 1 \right] (1 - \tau_d)^{-2}. \quad (22)$$

The moment of superfluidity onset can be easily calculated from the self-similar solutions as

$$\frac{t_d}{t_C}(\tau_d) = 1 + 6I_7(\delta(\tau_d), \tau_d), \quad (23)$$

where $I_7(\delta, \tau)$ is a rational integral for which an analytical expression is given in the appendix of Shternin & Yakovlev (2015). Finally, substitution of equation (23) into equation (20) results in an implicit equation on τ_d for a given $f_{\ell 0}$:

$$\xi \equiv f_{\ell 0} \left(\frac{\tilde{T}_d}{\tilde{T}_{\text{SC}}(t_d)} \right)^6 = \tau_d^6 \left[1 + 6I_7 \left(0.0085 \frac{12\tilde{s}/\xi - 1}{(1 - \tau_d)^2}, \tau_d \right) \right], \quad (24)$$

where

$$\tilde{s} = \frac{s_d}{2\beta}. \quad (25)$$

We denote the solution of equation (24) as $\tau_{\min}(\xi, \tilde{s})$; it can be easily found numerically. For convenience, we fit the solution $\tau_{\min}(\xi, \tilde{s})$ with the analytical expression given in Appendix D. The expression is valid for all $\xi < 1$ and $\tilde{s} \in 0.1 \dots 2$. The fit error does not exceed 4 per cent. For illustration, we plot the function $\tau_{\min}(\xi, \tilde{s})$ in Fig. 6 as a function of \tilde{s} for different values of ξ . According to Fig. 6, the dependence of τ_{\min} on \tilde{s} is quite modest for $\tilde{s} > 0.25$.

⁷ Notice that these values are 90 per cent limits on the universal limits but not on τ_d itself.

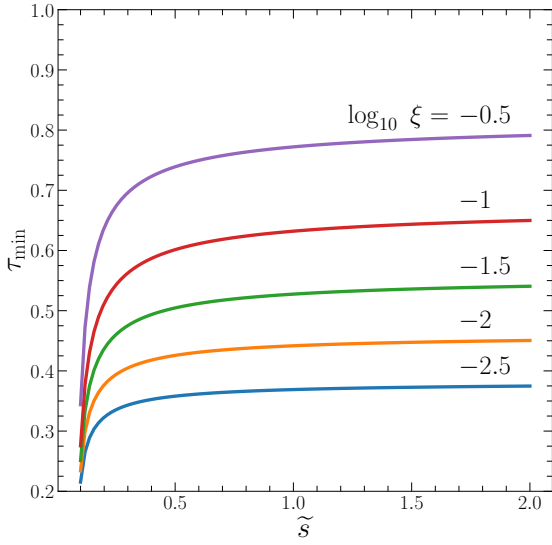


Figure 6. Function $\tau_{\min}(\xi, \tilde{s})$ as a function of \tilde{s} for different values of $\log_{10} \xi$ indicated near the curves.

Table 3. Possible ranges of τ_d and F_d parameters. qF_d^{low} and qF_d^{up} are the lower and upper boundaries, respectively, of the 90 per cent credible regions for qF_d . Upper and lower limits on τ_d and $\tilde{T}_{Cn\text{max}}$ correspond to the 90 per cent one-sided credible intervals for a corresponding quantity (see text for details). See Table 1 for definition of different models.

Model	qF_d^{low}	qF_d^{up}	τ_d^{low}	$q^{-1/5}\tau_d^{\text{up}}$	$q^{1/5}\tilde{T}_{Cn\text{max}}^{\text{low}}$ 10 ⁸ K	$\tilde{T}_{Cn\text{max}}^{\text{up}}$ 10 ⁸ K
1	0.34	1.10	0.45	0.90	3.3	6.6
2	0.32	0.98	0.44	0.91	3.2	6.7
3	0.62	1.23	0.44	0.81	3.2	6.1
4	0.59	1.10	0.43	0.82	3.1	6.1

The procedure outlined above allows one to constrain the lower boundary for τ_d . It is given by $\tau_d^{\text{low}} = \tau_{\min}(\xi_{nn}, \tilde{s})$, where ξ_{nn} is given by equation (24) with $f_{\ell 0} = f_{\ell nn}$. It is important to note that this lower limit does not depend on q . The 90 per cent one-sided credible interval for τ_d^{low} and the corresponding upper limit on the neutron superfluid critical temperature $\tilde{T}_{Cn\text{max}}^{\text{up}} = \tilde{T}_d/\tau_d^{\text{low}}$ are given in Table 3.

4.2.3 Combining all constraints

We summarize the results of Section 4.2 in Table 3 and Fig. 7. The boundaries of the 90 per cent credible intervals for qF_d [based on equation (16)] accompanied with the upper limit on $q^{-1/5}\tau_d$ [determined from equation (18)] and lower limit on τ_d [from the restriction $f_{\ell 0} > f_{\ell nn}$] define a box in the $\tau - F$ plane. It should be crossed by the $F(\tau)$ profile to successfully explain the cooling data on the CasA NS. For spectral model 1 (see Table 1 for definition), we plot these boxes for four values of $q = 1, 0.76, 0.4$ and 0.19 in Fig. 7; respective values of q are shown near the boxes. According

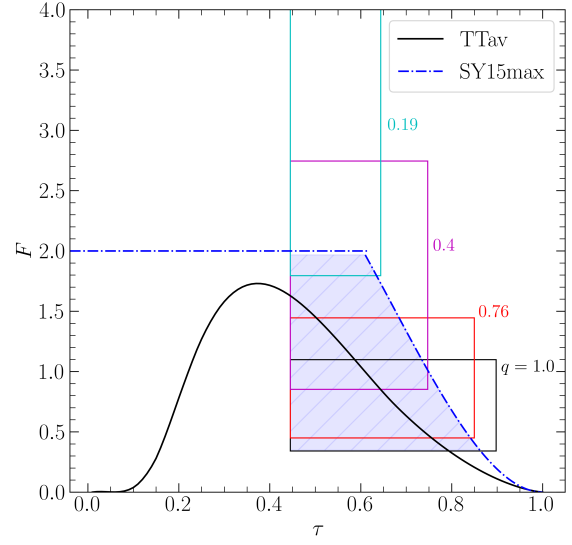


Figure 7. Restrictions on the allowed $\tau - F$ regions for different values of q for model 1 (variable N_H , no restrictions on the EOS). The solid line shows the same ‘TTav’ $F(\tau)$ profile as in Fig. 2. The dash-dotted broken curve limits the allowed region for $F(\tau)$ profiles.

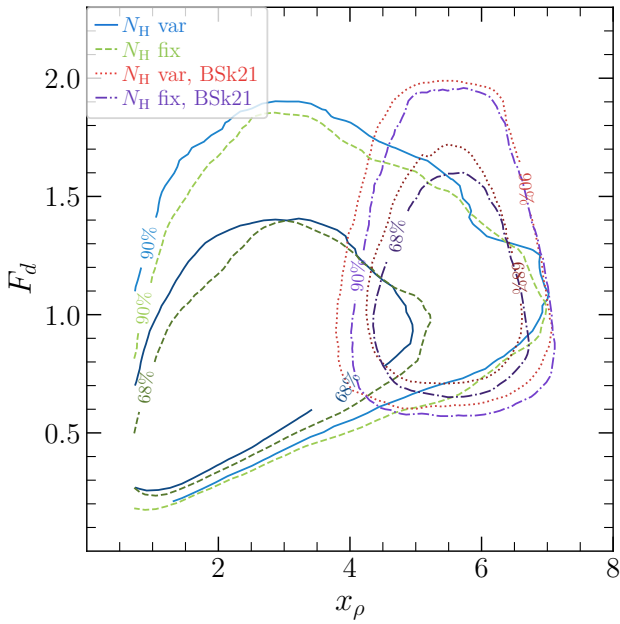
to the results of Section 3, any physically possible $F(\tau)$ profile lies below the broken dash-dotted curve, which combines the restrictions $F_d < F_{\text{max}} < 2$ and $F_d < F_{\text{SYmax}}(\tau_d)$ at $\tau_d > 0.6$. For illustration, in Fig. 7, as in Fig. 2, we show $F(\tau)$ for the ‘TTav’ superfluidity model by the black solid line. Therefore only a hatched area of each box for a given q can actually contain the allowed τ_d and F_d values. Notice that not all points from the hatched regions are equally probable, since the probability distribution of F_d , inferred from observations, is peaked near the median of the box. The $q = 0.19$ region is thus less probable that it may appear at first glance (see Section 4.3). The results of Section 4.2.2 show that a lower limit on τ_d does not depend on q . In contrast, decreasing q results in stronger constraints on τ_d from above, accompanied by stronger constraints on F_d from below. This requires fine tuning the superfluidity model [$F(\tau)$ profile] as Fig. 7 shows. As has already been anticipated from Fig. 5, the case $q = 0.19$ (Leinson 2010) can be only marginally reconciled with observations for spectral model 1.

4.3 Full Bayesian analysis

In the above analysis, we are basically unable to separate q and F_d . Moreover, the constraints described above do not fully take into account various correlations between the model parameters. In order to incorporate the mutual dependence of various quantities, we use the following Bayesian methodology. We add the unknown parameters q and τ_d to a set of the fit parameters. We assume a uniform prior distribution for q in the range 0 to 1 (we do not believe that the CPF mechanism would be stronger than the result of the non-covariant calculations) and a uniform prior on τ in the range 0.2 to 1. We apply the restrictions $F_d < F_{\text{max}} < 2$, $F_d < F_{\text{SYmax}}(\tau_d)$ [see equation (17)] and $f_{\ell 0} > f_{\ell nn}$ to the obtained multidimensional parameter distributions as described in Section 4.2.2 [i.e., $\tau_d > \tau_{\min}(\xi_{nn}, \tilde{s})$]. Credible intervals resulting from the marginalization

Table 4. Superfluidity model parameters. 68 per cent highest posterior density credible intervals are given. For the parameter q the 68 per cent (90 per cent) lower credible limits are shown instead. See Table 1 for definitions of different models.

Model	F_d	τ_d	x_ρ	δ	$\log_{10} f_{\ell 0}$	$\tilde{T}_{Cn\max}$ 10 ⁸ K	M M_\odot	R km	q
1	$0.77^{+0.42}_{-0.31}$	$0.57^{+0.12}_{-0.07}$	$1.5^{+2.2}_{-0.7}$	$3.4^{+3.2}_{-1.4}$	$-0.64^{+0.34}_{-0.68}$	$4.5^{+1.1}_{-0.5}$	$1.56^{+0.20}_{-0.22}$	$15.6^{+3.3}_{-3.0}$	> 0.61 (0.42)
2	$0.69^{+0.45}_{-0.26}$	$0.57^{+0.12}_{-0.08}$	$2.3^{+1.6}_{-1.4}$	$2.8^{+2.7}_{-1.1}$	$-0.70^{+0.42}_{-0.61}$	$4.4^{+1.1}_{-0.5}$	$1.60^{+0.20}_{-0.22}$	$14.8^{+3.6}_{-2.2}$	> 0.59 (0.40)
3	$1.00^{+0.41}_{-0.24}$	$0.53^{+0.11}_{-0.05}$	$5.6^{+0.6}_{-0.9}$	$4.1^{+4.8}_{-1.5}$	$-1.17^{+0.34}_{-0.47}$	$4.3^{+0.9}_{-0.5}$	$1.57^{+0.16}_{-0.25}$	12.6	> 0.67 (0.52)
4	$0.93^{+0.40}_{-0.23}$	$0.55^{+0.10}_{-0.08}$	$5.6^{+0.6}_{-0.8}$	$3.5^{+4.1}_{-1.3}$	$-1.19^{+0.46}_{-0.40}$	$4.4^{+0.7}_{-0.6}$	$1.64^{+0.12}_{-0.27}$	12.6	> 0.65 (0.49)

**Figure 8.** Posterior credible regions for the joint $F_d - x_\rho$ distribution for different spectral models. The contours correspond to 68 per cent and 90 per cent credibilities.

of the superfluidity parameters distribution obtained in this way are presented in Table 4. The marginalized 1D and 2D posterior distributions corresponding to Table 4 are shown in Figs. B3 and B4 in Appendix B.

The final constraint on τ_d for model 1 is $\tau_d = 0.57^{+0.12}_{-0.07}$ which translates into the maximal redshifted critical temperature of the triplet neutron superfluid of $\tilde{T}_{Cn\max} = 4.5^{+1.1}_{-0.5} \times 10^8$ K. The actual (non-redshifted) temperature $T_{Cn\max}$ is higher by a factor $e^{-\Phi}$, whose value depends on the position of the maximum of $T_{Cn}(\rho)$ within the NS core. Microscopic calculations typically find that this maximum is located at $\rho = (1-3)\rho_0$. In this range, $e^{-\Phi} = 1.2-1.8$, which gives $T_{Cn\max} \sim (5-10) \times 10^8$ K in accordance with previous results (e.g., Page et al. 2011; Shternin et al. 2011). In the unlikely case where the location of the maximum of $T_{Cn}(\rho)$ is deep in the interior of a very massive star, $T_{Cn\max}$ would be larger. However the lower limit on $T_{Cn\max}$ is robust. Notice that $\tilde{T}_{Cn\max}$ is quite well constrained independently of the particular EOS, superfluidity model or CPF neutrino emission suppression factor q , provided the last is not too small so that the CPF neutrino emission explanation of CasA NS cooling is still possible (see Fig. 7). Our solution constrains also the parameters δ and $f_{\ell 0}$ (see Table 4). Depending on the model, the maximal CPF cooling rate (parameter δ) should be

2 – 10 times stronger than slow cooling at superfluidity onset, and $f_{\ell 0}$ needs to be 2 – 40 times less powerful than the standard candle neutrino emission. This can be achieved by introducing proton superconductivity in a fraction of the core. Other models lead to compatible results. Notice that in this approach for all models, we find $q \gtrsim 0.4$ at 90 per cent credibility (see Table 4 and Figs. B3 and B4). According to the discussion at the end of Section 4.2.3, this is due to the lower plausibility of narrowing the τ_d range and having low F_d values at low q .

In Fig. 8, we show the 2D credible contours of F_d and x_ρ for the four models considered in the paper. More compact solutions (with larger x_ρ , i.e., BSk21-based models 3 and 4) require higher F_d . Fig. 8 should be compared to Fig. 3. Since $F_d < F_{\max}(x_\rho)$, those superfluid models for which the curves in Fig. 3 reside below the contours shown in Fig. 8 cannot provide successful fits to the CasA NS cooling data. These are the cases of the EEHOr and SYHHP pairing models. Other models can provide successful fits to the CasA data, until $x_\rho > 7$. The SYHHP model has been constructed phenomenologically by Shternin et al. (2011) in order to simultaneously explain the CasA cooling and other cooling neutron stars' data. However the cooling and spectral models in that work had not been treated self-consistently. The set of cooling curves was constructed for an EOS that leads to more compact neutron star models than the spectral fitting data actually suggests. This explains the failure of the SYHHP model found in a self-consistent study (Ho et al. 2015). However, a phenomenological model that explains all NS data can be easily constructed in a similar way to that done for SYHHP but based on less compact neutron star models.

5 DISCUSSION

Observations of the CasA NS constrain microphysical properties of NS superfluidity, in particular, the strength of the CPF neutrino emission encapsulated in the factor q [see equation (5)]. Our results imply that the current observational data do not allow q to be too small (see however the discussion below of the results of Posselt & Pavlov 2018). The strongest constraints on q come from the upper limit $F_d < 2$. According to equation (16), the constraints strongly depend on the model of the heat blanketing envelope (because of the factor \tilde{T}^5). Increasing the internal temperature \tilde{T} by only 10 per cent results in a factor 1.6 decrease of the lower limit on the q parameter. For the $T_s(T_b)$ dependence, we used the analytical approximations from Beznogov et al. (2016) instead of the exact calculations. However, their reported relative error does not exceed 2 per cent. Thus the approximation uncertainties in the $T_s(T_b)$ relation do not affect the conclusions on the q parameter, while a different heat blanketing envelope can change these conclusions.

Another source of systematics is the assumption of the minimal possible initial cooling rate ℓ_0 , which we take to be that of the

neutron-neutron bremsstrahlung of neutrino pairs. The rate for $f_{\ell\min}$ we employ is based on the calculations of Friman & Maxwell (1979) made in the framework of a one-pion exchange approximation for the strong interaction between neutrons. An increase of $f_{\ell nn}$ above these values increases τ_{\min} (Fig. 6). If τ_{\min} becomes $\gtrsim 0.6$, it starts to influence the possible range for q (see Fig. 7). According to Fig. 6, this can be important if $f_{\ell nn}$ is about three times higher than the adopted value. For not too low s_d , the minimal τ_d scales as $\tau_{\min} \propto f_{\ell nn}^{1/6}$.

The neutron-neutron bremsstrahlung rate can be considerably modified by in-medium effects. The simplest effect is that on the neutron effective mass which is set to $m_n^* = 0.7m_N$ in our calculations. In fact, m_n^* is uncertain, as are many other microscopic quantities in the NS core [including $T_{Cn}(\rho)$]. Each EOS model, in principle, should provide consistent m_n^* values. The models differ by the framework which is used to treat many-body effects, and by microphysical input to many-body theories. Even under the same many-body approach, the effective masses can vary by a considerable factor (e.g., Baldo et al. 2014). The neutrino cooling rate due to neutron-neutron bremsstrahlung is approximately proportional to the third power of effective mass, $\ell_{nn} \propto m_n^{*3}$. Therefore, roughly speaking, $\tau_{\min} \propto m_n^{*-1/2}$. Thus uncertainty of the effective mass modifies the upper limit on the maximal superfluid critical temperature $\tilde{T}_{Cn\max}$.

Other in-medium effects deal with the strong interaction beyond the in-vacuum one-pion exchange model (see, e.g., Schmitt & Shternin 2018, for review). The latter modifications are quite uncertain. For instance, using the free or in-medium scattering matrix in place of the one-pion exchange matrix element leads to the reduction of the nn bremsstrahlung rate by a factor of 2–4 (e.g., Van Dalen, Dieperink & Tjon 2003; Li et al. 2015). On the other hand, in the so-called ‘medium-modified one-pion exchange model’ (e.g., Voskresensky 2001), the bremsstrahlung rate is predicted to be increased by a factor of 100 at densities larger than the nuclear saturation density. Such a large initial cooling rate would be inconsistent with the CasA NS cooling mechanism analysed here.

The CPF neutrino emissivity in equations (5)–(6) is also affected by in-medium effects. To estimate the influence of m_n^* on the CPF rate is not straightforward, since it enters the denominator of equation (11) in a complex way. At the superfluidity onset, neutrons in the NS core dominate the heat capacity. Since the neutron contribution is proportional to m_n^* , the effective mass cancels out with the similar contribution to the numerator of equation (11). This holds until $\tau \gtrsim 0.5$, when the neutrons still dominate the heat capacity [in fact, just after the superfluidity onset the heat capacity of neutrons is enhanced (e.g. Yakovlev et al. 2001)]. At lower τ values, the neutron contribution to the heat capacity is suppressed, and ℓ_{CPF} starts to depend on m_n^* . However, these low τ values are not relevant for the CasA NS. Another influence of in-medium effects is that they can renormalize the coupling constants g_V and g_A (Migdal et al. 1990). In fact, all these effects are contained in the phenomenological parameter q . This should be kept in mind when the observed constraints on q are compared with the theoretical predictions. We also notice that the value $q = 0.19$ was obtained by Leinson (2010) in the strictly non-relativistic limit. However, the neutron Fermi velocity can be moderately large, i.e. $v_{Fn} \sim 0.3 - 0.7c$. The inclusion of relativistic corrections can potentially increase q , and the increase can be non-negligible.

There can be additional channels of energy losses. For instance, in addition to neutrino emission, axions can be emitted by the same processes. Axion emission during the CPF process increases the

total cooling rate, thus effectively increasing q . According to Leinson (2014) (see also Leinson 2021), this increase can be made quite strong. However, the axion-nucleon coupling leads to other emission processes, e.g., the CPF process due to proton pairing in the 1S_0 channel which can be stronger than the neutron bremsstrahlung luminosity (Hamaguchi et al. 2018). In this case, effectively increasing q by adding axions increases $f_{\ell\min}$ at the same time. As already pointed out, too large initial luminosity will be inconsistent with the CasA NS cooling in this model. The detailed study of axion cooling in the context of CasA NS observations deserves separate consideration (Hamaguchi et al. 2018).

In addition, there are indications (Posselt et al. 2013; Elshamouty et al. 2013; Posselt & Pavlov 2018) that the cooling of the CasA NS is weaker than inferred from the GRADED mode observations reported above and in Wijngaarden et al. (2019); Ho et al. (2021). Using FAINT subarray mode observations for three epochs, Posselt & Pavlov (2018) found $s_d = 0.53 \pm 0.19$ when N_H is allowed to vary between the epochs and $s_d = 0.36 \pm 0.15$ when N_H is fixed. These results are consistent within 1.3σ (depending on the model) with the results reported in Table 1. Nevertheless, these observations suggest a somewhat weaker cooling rate, with lower statistical significance [the probability to reject $s_d > 0.08$, i.e., the anomalous cooling, is 1 per cent (2.37σ) when N_H varies and 3 per cent (1.87σ) when N_H is constant]. One can estimate how the results of the analysis would change if the cooling slope is indeed smaller by some factor, than that obtained from the ACIS-S GRADED observations studied here. Indeed, the results of Section 2 show that the slope s weakly correlates with other spectral parameters (see Figs. B1 and B2). Therefore, in a first approximation we can rescale the s values to the ones obtained by Posselt & Pavlov (2018) leaving other parameters intact. According to equation (16), this weakens the constraints on q by about the same factor by which s decreases. This means that lowering s_d , as suggested by FAINT mode data, would make $q = 0.19$ more acceptable (see also Fig. 8 of Elshamouty et al. 2013). The limits on τ_d are rather weakly affected by s_d (see Section 4.2 and Fig. 6). Therefore, the constraints on the critical temperature would not change much, giving similar values to those in Table 4. Even lower cooling rates would still require the star to reside near the optimal $\tau_d \sim 0.5 - 0.6$ region of the cooling curve.

6 CONCLUSIONS

We derived semi-universal approximations for the integrated luminosity of the neutrino emission due to Cooper pair formation in the triplet channel of neutron pairing in the nucleon cores of NSs. The neutrino cooling rate in this process is given by equation (11) and contains two factors. The first factor depends on the model of the star and $T_{Cn\max}$ and can be described by the universal analytical expressions valid for a wide range of EOSs. The second factor, $F(\tau)$, depends on the shape of $T_{Cn}(\rho)$, as analysed here in detail for various EOSs and superfluidity models.

Using the constructed approximations and the self-similar cooling solutions from Shternin & Yakovlev (2015), we analysed the recent data on the cooling of the CasA NS from Wijngaarden et al. (2019); Ho et al. (2021). This approach allowed us to constrain the superfluid cooling solutions in a self-consistent way with the results of the spectral modelling. Provided the posterior distribution of the spectral model is known, one can constrain the parameters of the neutron superfluidity using the analytical expressions (16), (17) and

(D1). Also, these expressions allow one to analyse the dependence of the results on variations of the microphysics input.

Our main conclusions are as follows:

- The dimensionless function $F(\tau)$ depends on the model of the star, EOS and superfluidity. However, it is subject to model-independent constraints. Namely, it has a bell-like shape with the maximal value $F_{\max} < 2$, and at $\tau < 0.6$, it has the universal shape given by equation (13). The scaling parameter μ_{\max} in equation (13) is constrained as $\mu_{\max} < 0.18$.
- The spectral analysis of the CasA NS observations shows that the slope of the surface temperature decay is only weakly correlated with other model parameters, such as T , M or R .
- A large amount of light elements in the CasA NS envelope would contradict observations. This has already been mentioned previously (e.g., Shternin & Yakovlev 2015), but here we show that this result is robust.
- The maximal redshifted critical temperature of the triplet neutron superfluid is well-constrained in the range $\bar{T}_{Cn\max} = 4.5^{+1.1}_{-0.5} \times 10^8$ K independently of the particular model of nucleon NS cores. This constraint will not be strongly modified if the actual CasA NS cooling is actually weaker but still faster than the standard one. The non-redshifted maximal critical temperature is then constrained to be $T_{Cn\max} \sim (5 - 10) \times 10^8$ K for realistic $T_{Cn}(\rho)$. Recently Kantor, Gusakov & Dommes (2020) obtained similar constraints on the maximal critical temperature of neutrons [namely, $T_{Cn\max} > (3 - 6) \times 10^8$ K] from their analysis of the physics of r-modes. These quite different insights into neutron star interiors give compatible results.
- The integrated rate of the CPF mechanism can be described by the phenomenological factor q . We find that the current data suggests that $q \gtrsim 0.4$ at 90 per cent credibility, which is about twice as high as the results of Leinson (2010). If our model is correct, this may indicate that either there are still some systematic effects unaccounted for in the data analysis which result in overestimation of the actual CasA NS cooling or additional theoretical factors are present which strengthen the CPF neutrino emission mechanism, for instance due to relativistic or in-medium corrections, or other energy loss channels, such as the axion emission.

ACKNOWLEDGEMENTS

This work is supported by the Russian Science Foundation, grant 19-12-00133. The authors are grateful to Dima Yakovlev for numerous discussions. WCGH appreciates use of computer facilities at the Kavli Institute for Particle Astrophysics and Cosmology. COH is supported by the Natural Sciences and Engineering Research Council of Canada (NSERC) via Discovery Grant RGPIN-2016-04602.

DATA AVAILABILITY

The data underlying this article will be shared on reasonable request to the corresponding author.

REFERENCES

Andrae R., Schulze-Hartung T., Melchior P., 2010, arXiv:1012.3754,
 Arnaud K. A., 1996, in Jacoby G. H., Barnes J., eds, *Astronomical Society of the Pacific Conference Series Vol. 101, Astronomical Data Analysis Software and Systems V*. p. 17

Ashworth W. B. J., 1980, *Journal for the History of Astronomy*, 11, 1
 Baldo M., Burgio G. F., Schulze H.-J., Taranto G., 2014, *Phys. Rev. C*, 89, 048801
 Beznogov M. V., Potekhin A. Y., Yakovlev D. G., 2016, *MNRAS*, 459, 1569
 Blaschke D., Grigorian H., Voskresensky D. N., Weber F., 2012, *Phys. Rev. C*, 85, 022802
 Blaschke D., Grigorian H., Voskresensky D. N., 2013, *Phys. Rev. C*, 88, 065805
 Bonanno A., Baldo M., Burgio G. F., Urpin V., 2014, *A&A*, 561, L5
 Cash W., 1979, *ApJ*, 228, 939
 Chang P., Bildsten L., 2003, *ApJ*, 585, 464
 Chang P., Bildsten L., Arras P., 2010, *ApJ*, 723, 719
 van Dalen E. N., Dieperink A. E., Tjon J. A., 2003, *Phys. Rev. C*, 67, 065807
 Davis J. E., 2001, *ApJ*, 562, 575
 Doroshenko V., Suleimanov V., Santangelo A., 2018, *A&A*, 618, A76
 Elshamouty K. G., Heinke C. O., Sivakoff G. R., Ho W. C. G., Shternin P. S., Yakovlev D. G., Patnaude D. J., David L., 2013, *ApJ*, 777, 22
 Fesen R. A., et al., 2006, *ApJ*, 645, 283
 Flowers E., Ruderman M., Sutherland P., 1976, *ApJ*, 205, 541
 Foreman-Mackey D., Hogg D. W., Lang D., Goodman J., 2013, *PASP*, 125, 306
 Friman B. L., Maxwell O. V., 1979, *ApJ*, 232, 541
 Fruscione A., et al., 2006, in Silva D. R., Doxsey R. E., eds, *Society of Photo-Optical Instrumentation Engineers (SPIE) Conference Series Vol. 6270*, Society of Photo-Optical Instrumentation Engineers (SPIE) Conference Series. p. 62701V
 Gnedin O. Y., Yakovlev D. G., Potekhin A. Y., 2001, *MNRAS*, 324, 725
 Green D. A., Stephenson F. R., 2003, in Weiler K., ed., *Lecture Notes in Physics Vol. 598, Supernovae and Gamma-Ray Bursters*. pp 7–19
 Grigorian H. A., Blaschke D. B., Voskresensky D. N., 2014, *Journal of Physics Conference Series*, 496, 012014
 Gudmundsson E. H., Pethick C. J., Epstein R. I., 1983, *ApJ*, 272, 286
 Gusakov M. E., Kaminker A. D., Yakovlev D. G., Gnedin O. Y., 2004, *A&A*, 423, 1063
 Gusakov M. E., Kaminker A. D., Yakovlev D. G., Gnedin O. Y., 2005, *MNRAS*, 363, 555
 Hamaguchi K., Nagata N., Yanagi K., Zheng J., 2018, *Phys. Rev. D*, 98, 103015
 Haskell B., Sedrakian A., 2018, in Rezzolla L., Pizzochero P., Jones D. I., Rea N., Vidaña I., eds, *The Physics and Astrophysics of Neutron Stars*. Springer International Publishing, Cham, pp 401–454
 Hebbard P. R., Heinke C. O., Ho W. C. G., 2020, *MNRAS*, 491, 1585
 Heinke C. O., Ho W. C. G., 2010, *ApJ*, 719, L167
 Ho W. C. G., Heinke C. O., 2009, *Nature*, 462, 71
 Ho W. C. G., Elshamouty K. G., Heinke C. O., Potekhin A. Y., 2015, *Phys. Rev. C*, 91, 015806
 Ho W. C. G., Zhao Y., Heinke C. O., Kaplan D. L., Shternin P. S., Wijngaarden M. J. P., 2021, *MNRAS*, submitted
 Kantor E. M., Gusakov M. E., Dommes V. A., 2020, *Phys. Rev. Lett.*, 125, 151101
 Klochkov D., Pühlhofer G., Suleimanov V., Simon S., Werner K., Santangelo A., 2013, *A&A*, 556, A41
 Klochkov D., Suleimanov V., Sasaki M., Santangelo A., 2016, *A&A*, 592, L12
 Kundu J., Reddy S., 2004, *Phys. Rev. C*, 70, 055803
 Lattimer J. M., Prakash M., 2016, *Phys. Rep.*, 621, 127
 Leinson L. B., 2010, *Phys. Rev. C*, 81, 025501
 Leinson L. B., 2014, *J. Cosmology Astropart. Phys.*, 2014, 031
 Leinson L. B., 2018, *Advances in High Energy Physics*, 2018, 8963453
 Leinson L. B., 2021, preprint (arXiv:2105.14745)
 Leinson L. B., Pérez A., 2006, *Physics Letters B*, 638, 114
 Li Y., Liou M. K., Schreiber W. M., Gibson B. F., 2015, *Phys. Rev. C*, 92, 015504
 Migdal A. B., Saperstein E. E., Troitsky M. A., Voskresensky D. N., 1990, *Phys. Rep.*, 192, 179
 Miller M. C., et al., 2019, *ApJ*, 887, L24
 Negreiros R., Schramm S., Weber F., 2013, *Physics Letters B*, 718, 1176
 Nomoto K., Tsuruta S., 1981, *ApJ*, 250, L19

Ofengeim D. D., Yakovlev D. G., 2017a, MNRAS, 467, 3598
 Ofengeim D. D., Yakovlev D. G., 2017b, Journal of Physics Conference Series, 932, 012049
 Ofengeim D., Zyuzin D., 2018, Particles, 1, 14
 Ofengeim D. D., Kaminker A. D., Klochkov D., Suleimanov V., Yakovlev D. G., 2015, MNRAS, 454, 2668
 Ofengeim D. D., Fortin M., Haensel P., Yakovlev D. G., Zdunik J. L., 2017, Phys. Rev. D, 96, 043002
 Page D., Lattimer J. M., Prakash M., Steiner A. W., 2004, ApJS, 155, 623
 Page D., Lattimer J. M., Prakash M., Steiner A. W., 2009, ApJ, 707, 1131
 Page D., Prakash M., Lattimer J. M., Steiner A. W., 2011, Physical Review Letters, 106, 081101
 Pavlov G. G., Zavlin V. E., Aschenbach B., Trümper J., Sanwal D., 2000, ApJ, 531, L53
 Posselt B., Pavlov G. G., 2018, ApJ, 864, 135
 Posselt B., Pavlov G. G., Suleimanov V., Kargaltsev O., 2013, ApJ, 779, 186
 Potekhin A. Y., Chabrier G., 2018, A&A, 609, A74
 Potekhin A. Y., Chabrier G., Yakovlev D. G., 1997, A&A, 323, 415
 Potekhin A. Y., Yakovlev D. G., Chabrier G., Gnedin O. Y., 2003, ApJ, 594, 404
 Potekhin A. Y., Fantina A. F., Chamel N., Pearson J. M., Goriely S., 2013, A&A, 560, A48
 Potekhin A. Y., Pons J. A., Page D., 2015, Space Science Reviews, 191, 239
 Reed J. E., Hester J. J., Fabian A. C., Winkler P. F., 1995, ApJ, 440, 706
 Richardson M. B., van Horn H. M., Ratcliff K. F., Malone R. C., 1982, ApJ, 255, 624
 Riley T. E., et al., 2019, ApJ, 887, L21
 Schmitt A., Shternin P., 2018, in Rezzolla L., Pizzochero P., Jones D. I., Rea N., Vidana I., eds, The Physics and Astrophysics of Neutron Stars. Springer International Publishing, Cham, pp 455–574
 Sedrakian A., 2013, A&A, 555, L10
 Shternin P. S., Yakovlev D. G., 2008, Astronomy Letters, 34, 675
 Shternin P. S., Yakovlev D. G., 2015, MNRAS, 446, 3621
 Shternin P. S., Yakovlev D. G., Heinke C. O., Ho W. C. G., Patnaude D. J., 2011, MNRAS, 412, L108
 Suleimanov V. F., Klochkov D., Pavlov G. G., Werner K., 2014, ApJS, 210, 13
 Takatsuka T., Tamagaki R., 2004, Progress of Theoretical Physics, 112, 37
 Tananbaum H., 1999, IAU Circ., 7246, 1
 Thorne K. S., 1966, in Gratton L., ed., Proceedings of the International School of Physics "Enrico Fermi," Course XXXV, at Varenna, Italy, July 12–24, 1965. Academic Press, New York, pp 166–280
 Voskresensky D. N., 2001, in Blaschke D., Glendenning N. K., Sedrakian A., eds, Lecture Notes in Physics, Berlin Springer Verlag Vol. 578, Physics of Neutron Star Interiors. p. 467
 Wijngaarden M. J. P., Ho W. C. G., Chang P., Heinke C. O., Page D., Beznogov M., Patnaude D. J., 2019, MNRAS, 484, 974
 Wijngaarden M. J. P., et al., 2020, MNRAS, 493, 4936
 Wilms J., Allen A., McCray R., 2000, ApJ, 542, 914
 Yakovlev D. G., Pethick C. J., 2004, Ann. Rev. Astron. Astrophys., 42, 169
 Yakovlev D. G., Kaminker A. D., Gnedin O. Y., Haensel P., 2001, Phys. Rep., 354, 1
 Yakovlev D. G., Ho W. C. G., Shternin P. S., Heinke C. O., Potekhin A. Y., 2011, MNRAS, 411, 1977
 Yang S.-H., Pi C.-M., Zheng X.-P., 2011, ApJ, 735, L29

APPENDIX A: C-STATISTICS FOR UNBINNED DATA

When fitting unbinned data with C -statistics, we found systematically lower values of the NS radius (i.e. around 9 km) than those obtained with the data binned by 25 cnts/bin and χ^2 statistics, or by using the C -statistics but with the data binned by 1 cnt/bin. Therefore we performed the following bootstrap test. Starting from some selected values of parameters, close to the best-fit values described in the paper, we simulated $N_{\text{boot}} = 100$ sets of CasA NS spectra using the `xSPEC` tool `FAKEIT`. We simulated either unbinned spectra,

Table B1. Mean autocorrelation time τ_{acor} , number of chain steps N_{steps} and number of parameters N_{par} for four spectral models.

Model	τ_{acor}	N_{steps}	N_{par}
1	3900	230000	35
2	950	57000	20
3	1600	127000	34
4	950	38000	19

spectra binned by a minimum of 1 count per energy bin and spectra binned by a minimum of 25 counts per bin. Then we fitted (with `xSPEC`) the resulting fake spectra using C -statistics in the first two cases, and χ^2 statistics in the last one. Since we are mainly interested in R , to reduce the computational cost, we fixed $M = 1.6 M_{\odot}$, $d = 3.4$ kpc, and tied N_H between all observations. In addition, we reduced the number of pileup grade migration parameters α to two values, one for observations with frame times of 3.24 s and another for observations with frame times of 3.04 s (e.g., Ho & Heinke 2009). We checked that the fit converged to the correct minimum using the `STEPPAR` command over R . In this way we obtained the bootstrap distributions of R values shown in Fig. A1. One expects that the inferred values are distributed around the true value that, for the case shown in Fig. A1, was $R = 16.4$ km, as shown with vertical lines. Indeed, when the simulated data was binned by 25 counts per bin and χ^2 statistics was used, the resulting histogram of inferred R is centered around the true value (see left panel of Fig. A1). The histogram recovered in the case of 1 count per bin data binning and C -statistics is less symmetric but still looks reasonable (see right panel of Fig. A1). In contrast the results for the unbinned data using C -statistics are strongly biased. According to the middle panel of Fig. A1, all the simulated spectra were fitted by far smaller radii than the true value. We therefore conclude that our data is another example⁸ when the use of the C -statistics with unbinned data require special care and can lead to strongly biased results.

APPENDIX B: POSTERIOR DISTRIBUTIONS AND NUISANCE PARAMETERS.

We fitted the spectra using the affine-invariant MCMC sampler `emcee`. Since the number of fitting parameters is relatively large, we used 128 walkers. The number of steps in the chains varied depending on the mean autocorrelation time τ_{acor} . We ensured that the number of steps N_{steps} was greater than $50 \times \tau_{\text{acor}}$ and that the τ_{acor} estimate from the chain was stable. Typically, for larger numbers of fit parameters τ_{acor} increases. The mean autocorrelation times and numbers of chain steps for models 1...4 are given in Table B1. The final $5 \times \tau_{\text{acor}}$ steps were left for inferences and each 10th sample was used.

The marginalized posterior distributions for spectral models 1 and 2 are shown in Fig. B1, while the distributions for models 3 and 4 are shown in Fig. B2. Analogous distributions of the superfluidity parameters are shown in Figs. B3 (models 1 and 2) and B4 (models 3 and 4). In each figure, solid lines/contours correspond to a model with variable N_H , while dashed lines/contours correspond to

⁸ See the discussion in the `xSPEC` manual, <https://heasarc.gsfc.nasa.gov/xanadu/xspec/manual/node312.html>.

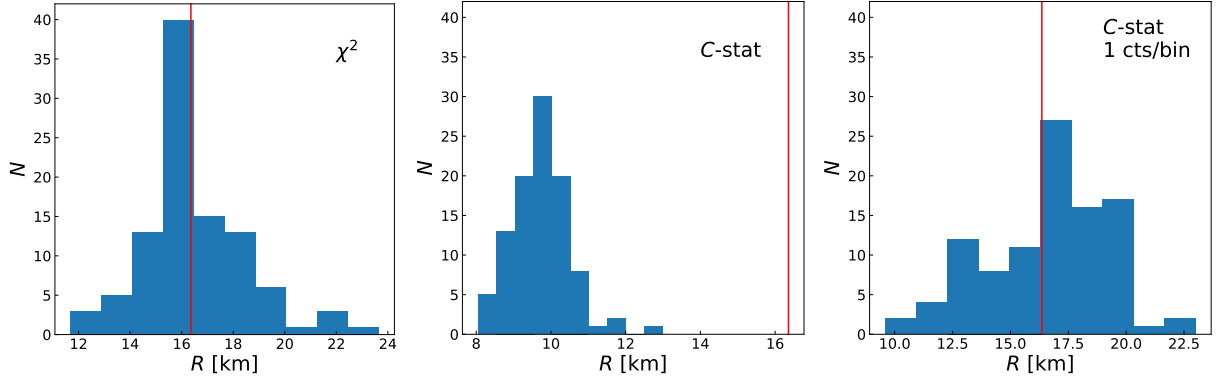


Figure A1. Bootstrap distribution of the NS radius R for different fit statistics (left: χ^2 , middle: C -stat, unbinned data, right: C -stat, data binned by 1 cnts/bin). Vertical line in each plot shows the ‘true’ value of $R = 16.3$ km.

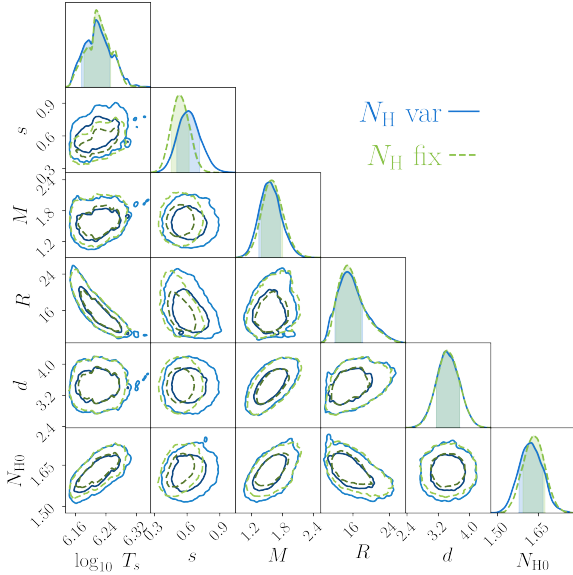


Figure B1. Posteriors for spectral parameters for models 1 and 2 with no restrictions on the EOS. Model 1 is shown with solid lines while model 2 - with dashed lines.

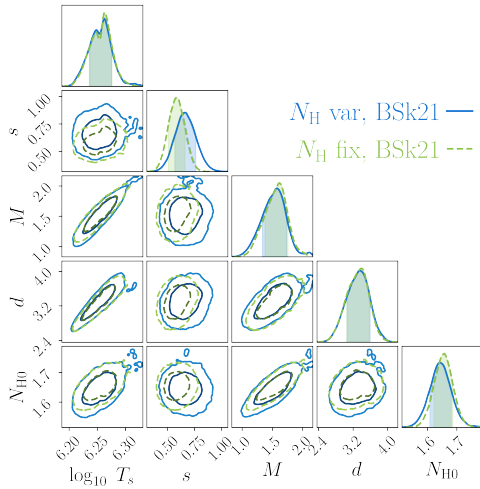


Figure B2. Posteriors for spectral parameters for models 3 and 4 which correspond to the BSk21 EOS. Model 3 is shown with solid lines while model 4 is shown with dashed lines.

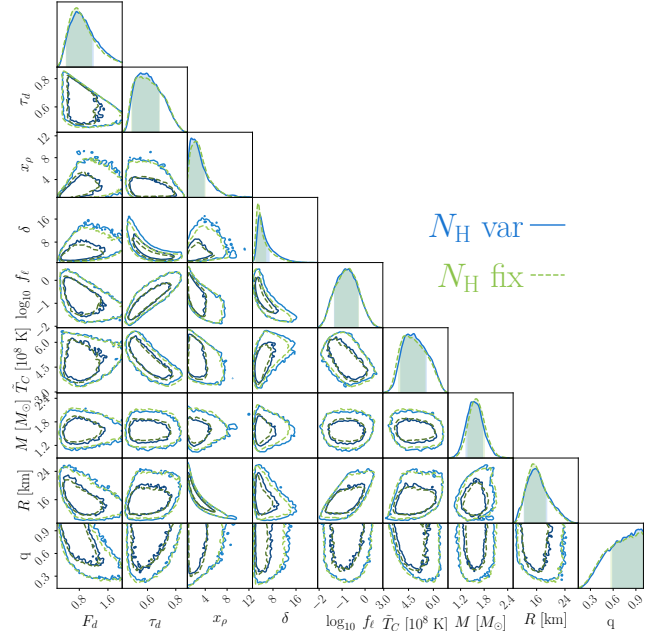


Figure B3. Posteriors for superfluidity parameters for models 1 and 2 with no restrictions on the EOS. Model 1 is shown with solid lines while model 2 with dashed lines.

a model with fixed N_H . The inner and outer 2D contours correspond to 68 and 90 per cent credibility, respectively, while the 68 per cent highest posterior density credible intervals are shaded in 1D plots.

We do not show posteriors for the N_{Hi} and α_i parameter sets for simplicity; the summary of their inferences are given in Table B2.

APPENDIX C: EXPLICIT EXPRESSIONS FOR THE FUNCTIONS $J_{1,5}$ AND $J_{1,1}$

According to Ofengeim et al. (2017), the integral-like equation (8) could be approximated by the expression (9), where the function $J_{1,5}$ belongs to the family

$$J_{k,p}(M, R) = a_1 \zeta^{k-3} \frac{x_\rho^{k/3} \left[1 + (a_2 x_\rho \zeta^3)^{\gamma-1} \right]^{\frac{p\gamma-k/3}{\gamma-1}}}{(1-x_g)^{p/2} \sqrt{1-a_5 x_g}}, \quad (C1)$$

Table B2. Grade migration parameters α and absorption column densities $N_{\text{H},22}$ (10^{22} cm^{-2}) (for models 1 and 3 only). For merged ObsIDs, the MJD listed is that of the first ObsID. Uncertainties correspond to the 68 per cent highest posterior density credible intervals.

ObsID	Date	MJD	Model 1		Model 2	Model 3		Model 4
			$N_{\text{H},22}$	α	α	$N_{\text{H},22}$	α	α
114	2000 Jan 30	51573.4	$1.63^{+0.05}_{-0.04}$	$0.40^{+0.06}_{-0.05}$	$0.42^{+0.05}_{-0.05}$	$1.66^{+0.04}_{-0.04}$	$0.38^{+0.04}_{-0.04}$	$0.39^{+0.04}_{-0.04}$
1952	2002 Feb 6	52311.3	$1.64^{+0.05}_{-0.05}$	$0.37^{+0.05}_{-0.06}$	$0.38^{+0.05}_{-0.05}$	$1.66^{+0.04}_{-0.04}$	$0.33^{+0.05}_{-0.04}$	$0.35^{+0.04}_{-0.04}$
5196	2004 Feb 8	53043.7	$1.60^{+0.05}_{-0.04}$	$0.34^{+0.05}_{-0.05}$	$0.35^{+0.05}_{-0.05}$	$1.63^{+0.04}_{-0.04}$	$0.36^{+0.04}_{-0.04}$	$0.32^{+0.04}_{-0.05}$
9117/9773	2007 Feb 5/8	54439.9	$1.66^{+0.04}_{-0.06}$	$0.39^{+0.07}_{-0.05}$	$0.41^{+0.05}_{-0.06}$	$1.68^{+0.04}_{-0.05}$	$0.37^{+0.05}_{-0.05}$	$0.37^{+0.05}_{-0.05}$
10935/12020	2009 Nov 2/3	55137.9	$1.63^{+0.05}_{-0.04}$	$0.34^{+0.06}_{-0.07}$	$0.33^{+0.06}_{-0.06}$	$1.66^{+0.04}_{-0.04}$	$0.36^{+0.05}_{-0.05}$	$0.31^{+0.05}_{-0.05}$
10936/13177	2010 Oct 31/Nov 2	55500.2	$1.64^{+0.04}_{-0.06}$	$0.30^{+0.06}_{-0.06}$	$0.30^{+0.06}_{-0.06}$	$1.65^{+0.04}_{-0.04}$	$0.26^{+0.05}_{-0.05}$	$0.27^{+0.05}_{-0.05}$
14229	2012 May 15	56062.4	$1.67^{+0.04}_{-0.06}$	$0.22^{+0.07}_{-0.09}$	$0.20^{+0.08}_{-0.07}$	$1.69^{+0.04}_{-0.04}$	$0.16^{+0.07}_{-0.06}$	$0.16^{+0.07}_{-0.06}$
14480	2013 May 20	56432.6	$1.61^{+0.05}_{-0.05}$	$0.30^{+0.07}_{-0.07}$	$0.32^{+0.06}_{-0.08}$	$1.64^{+0.04}_{-0.04}$	$0.26^{+0.05}_{-0.06}$	$0.27^{+0.05}_{-0.06}$
14481	2014 May 12	56789.1	$1.64^{+0.05}_{-0.04}$	$0.19^{+0.08}_{-0.07}$	$0.19^{+0.07}_{-0.07}$	$1.67^{+0.04}_{-0.05}$	$0.15^{+0.06}_{-0.06}$	$0.15^{+0.06}_{-0.05}$
14482	2015 Apr 30	57142.5	$1.61^{+0.05}_{-0.05}$	$0.21^{+0.06}_{-0.08}$	$0.20^{+0.07}_{-0.07}$	$1.63^{+0.04}_{-0.05}$	$0.16^{+0.06}_{-0.06}$	$0.16^{+0.07}_{-0.05}$
19903/18344	2016 Oct 20/21	57681.2	$1.59^{+0.05}_{-0.05}$	$0.19^{+0.07}_{-0.08}$	$0.18^{+0.07}_{-0.07}$	$1.62^{+0.04}_{-0.05}$	$0.16^{+0.05}_{-0.07}$	$0.13^{+0.07}_{-0.06}$
19604	2017 May 16	57889.7	$1.60^{+0.06}_{-0.05}$	$0.20^{+0.07}_{-0.08}$	$0.19^{+0.08}_{-0.07}$	$1.63^{+0.04}_{-0.05}$	$0.16^{+0.06}_{-0.07}$	$0.15^{+0.06}_{-0.06}$
19605	2018 May 15	58253.7	$1.56^{+0.06}_{-0.05}$	$0.14^{+0.10}_{-0.05}$	$0.16^{+0.09}_{-0.07}$	$1.60^{+0.04}_{-0.06}$	$0.12^{+0.08}_{-0.06}$	$0.12^{+0.07}_{-0.07}$
19606	2019 May 13	58616.5	$1.61^{+0.06}_{-0.05}$	$0.19^{+0.11}_{-0.06}$	$0.20^{+0.08}_{-0.09}$	$1.64^{+0.04}_{-0.05}$	$0.17^{+0.06}_{-0.09}$	$0.16^{+0.07}_{-0.08}$

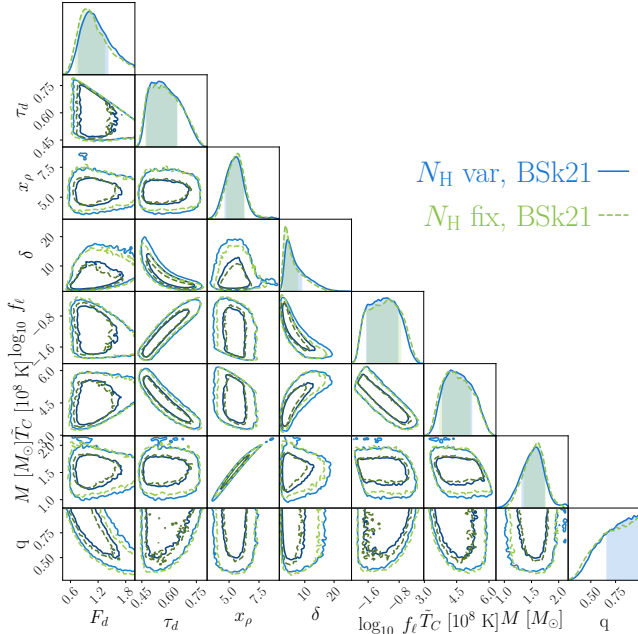


Figure B4. Posteriors for superfluidity parameters for models 3 and 4 which correspond to the BSk21 EOS. Model 3 is shown with solid lines while model 4 with dashed lines.

where $x_g = 2GM/(Rc^2)$, $x_\rho = M/(\rho_0 R^3)$, $\zeta(M, R) \approx 0.0582/x_g + 0.9418$, and

$$\gamma = a_3 \left(1 + a_4 \xi \sqrt{x_g^5/x_\rho} \right)^{-1}. \quad (\text{C2})$$

Further, $k/3$ is a power index in the number density dependence of the factor before the fraction in equation (8) (in our case, $k = 1$), p is the factor in the redshift exponent in equation (8) (in our case, $p = 5$), and $a_1 \dots a_5$ are the fitting parameters.

In the case of equation (9), the latter ones were fitted to the same set of EOS models as in Ofengeim et al.

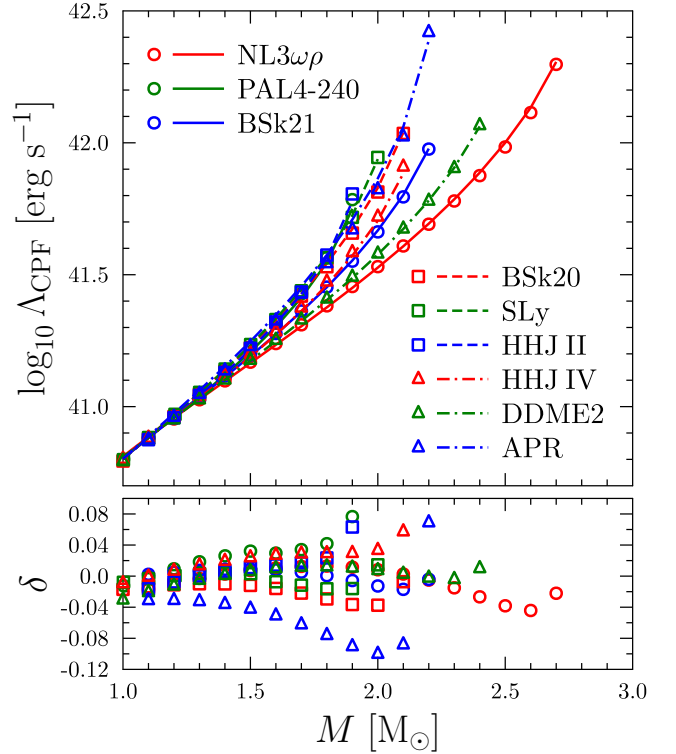


Figure C1. Top: comparison of numerically calculated Λ_{CPF} and its approximation (9). Bottom: relative deviations δ between the fit and numerical data.

(2017). The best-fit values appear to be $\{a_1, a_2, a_3, a_4, a_5\} = \{14.63, 0.0104, 2.65, 3.89, 0.800\}$, the root mean square relative error is 3% and the maximum relative deviation is 10%. Therefore, the approximation given by equations (9), (C1) is rather accurate, as additionally verified by Fig. C1.

As detailed in Ofengeim et al. (2017), the heat capacity can be fitted in a similar way [see the text before equation (10)]

but requires $p = 1$. In the case ‘ $n\ell$ ’, which we are interested in here, the fitting parameters are $\{a_1, a_2, a_3, a_4, a_5\} = \{3.01, 0.0130, 2.59, 3.50, 0.799\}$, the root mean square relative error is 1.5% and the maximum relative deviation is 4.7%.

APPENDIX D: EXPLICIT APPROXIMATION FOR THE FUNCTION $\tau_{\min}(\xi, \tilde{s})$

We approximate the solution of the equation (24) in the following way:

$$\tau_{\min}(\xi, \tilde{s}) = \left[(1+a) \xi^{p/6} - a \right]^{1/p}, \quad (\text{D1})$$

where

$$p = -6 \frac{\ln \arctan \sqrt{\lambda} - \ln \sqrt{\lambda}}{\ln(1+\lambda)} + \ln \left[1 + \left(\frac{\lambda}{b_1} \right)^{b_2} \right], \quad (\text{D2})$$

$$a = \frac{(1+\lambda)^{p/6}}{(1+\lambda)^{p/6} - 1}, \quad (\text{D3})$$

$$\lambda = 12 \frac{\tilde{s}}{\xi} - 1. \quad (\text{D4})$$

For the ranges $\tilde{s} = 0.1 \dots 2$ and $\log_{10} \xi = -4 \dots 0$, the fitting parameters $b_{1,2}$ have the best-fit values $b_1 = 100$ and $b_2 = 0.527$, with the rms error 0.005 and the maximum error 0.04 at the lowest values of \tilde{s} . For $\tilde{s} > 0.3$ that is relevant for CasA NS, the absolute maximum error does not exceed 0.01.

This paper has been typeset from a \LaTeX file prepared by the author.